Subsample averaging for non-periodic microstructures: bias reduction, dispersion increase, and practical trade-offs in computational micromechanics

Tim Sentler[1], Peter Bella[2], and Matti Schneider[1,3,4*]

[1]University of Duisburg-Essen, Institute of Engineering Mathematics
[2]TU Dortmund, School of Mathematics
[3]Center for Nanointegration Duisburg-Essen (CENIDE)
[4]Fraunhofer Institute for Industrial Mathematics ITWM, Kaiserslautern
[*]correspondence to: matti.schneider@uni-due.de

Author Accepted Manuscript

This is the author-accepted version of the article

T. Sentler, P. Bella, and M. Schneider, "Subsample averaging for non-periodic microstructures: bias reduction, dispersion increase, and practical trade-offs in computational micromechanics," *European Journal of Mechanics – A/Solids*, Article 106363 (2026).

The Version of Record is available at https://doi.org/10.1016/j.euromechsol.2026.106363.

This manuscript includes all revisions accepted following peer review, but does not include the publisher's copy-editing, typesetting, pagination, or other production changes.

The research of TS and MS has received funding from the European Research Council (ERC) under the European Union's Horizon Europe research and innovation programme under grant agreement No. 101040238 (*BeyondRVE*).

Abstract

The computation of effective properties of random microstructured materials via representative volume elements (RVE) is affected by both bias and dispersion. For non-periodic microstructures (snapshots), which naturally arise in experiments and imaging-based studies, the bias decays slowly, rendering standard homogenization approaches inaccurate, significantly biased, and therefore unreliable. Recent theoretical results suggest that subsample averaging – evaluating the apparent properties only on a strictly interior subdomain – can significantly reduce the bias. In this work, we investigate the practical performance of subsample averaging for linear elastic particle-reinforced composites using large-scale numerical experiments and FFT-based computational micromechanics.

We first demonstrate that subsample averaging must respect the Hill-Mandel condition to improve the convergence behavior of the bias, i.e., both stress and strain fields must be subsample averaged.

In particular, the naive approach of subsample averaging the apparent stress alone may reduce the magnitude of the bias, but does not improve its convergence rate. When applied consistently, subsample averaging reduces the magnitude of the bias and produces a more favorable decay trend for the investigated non-periodic microstructures. However, this bias reduction comes at the cost of an increased dispersion due to the reduced sampling domain, resulting in only marginal improvements of the total error when used in isolation.
To overcome this limitation, we combine subsample averaging with variance reduction via optimized volume fraction (OVF), which significantly improves overall accuracy and reliability for matrix-inclusion composites. The presented strategy is straightforward to implement and can be readily applied within existing computational frameworks without modifying the underlying solver.
These results reveal a fundamental bias–dispersion trade-off associated with subsample averaging and provide practical guidance for computing the effective properties from non-periodic microstructure samples, including samples obtained experimentally.

Keywords: Representative volume element; Subsample averaging; Non-periodic microstructures; Computational micromechanics; Stochastic homogenization; Variance reduction

1 Introduction

1.1 Sources of error in representativity studies

Computing effective material properties of heterogeneous media by means of representative volume elements (RVE) [1, 2] is a central task in computational homogenization [3–5]. In practice, the underlying microstructures are often obtained from imaging techniques such as tomography scans or microscopy [6,7]. These data provide finite samples of the material, commonly referred to as snapshots, which are inherently non-periodic.
A key difficulty in this setting is that the apparent properties computed on finite samples deviate from the effective properties of the underlying infinite medium. Following the framework of stochastic homogenization [8–10], this discrepancy can be decomposed into a dispersion, also referred to as random error in the literature, describing the fluctuations between realizations, and a systematic error, also referred to in the literature as bias, describing the deviation of the ensemble mean from the effective properties. While the dispersion can be estimated and controlled by sampling strategies [11, 12], the bias is more difficult to quantify in practice.

1.2 Periodized versus non-periodic samples

A fundamental distinction arises between periodized ensembles and non-periodic samples (snapshots), illustrated in Fig. 1. In the periodized case, the microstructure is constructed such that periodic extension does not introduce inconsistencies across the boundary. In contrast, snapshot microstructures are obtained by cutting a finite sample from a larger realization, which generally leads to discontinuities at the boundary. These boundary inconsistencies are a primary source of the increased bias observed for snapshot microstructures. More precisely, for periodized ensembles, the bias typically exhibits fast decay with increasing unit cell size - independent of the applied boundary conditions for the displacement fluctuation. In contrast, for snapshot microstructures, the bias is significantly larger and decays more slowly [13]. As a consequence, computing the apparent properties of experimentally obtained microstructures naively may lead to unreliable results, even for comparatively large sample sizes [14–16].
To put these works in perspective: The decomposition of the homogenization error into a bias and a random contribution was already established [11]. Also, the superiority of periodized microstructures

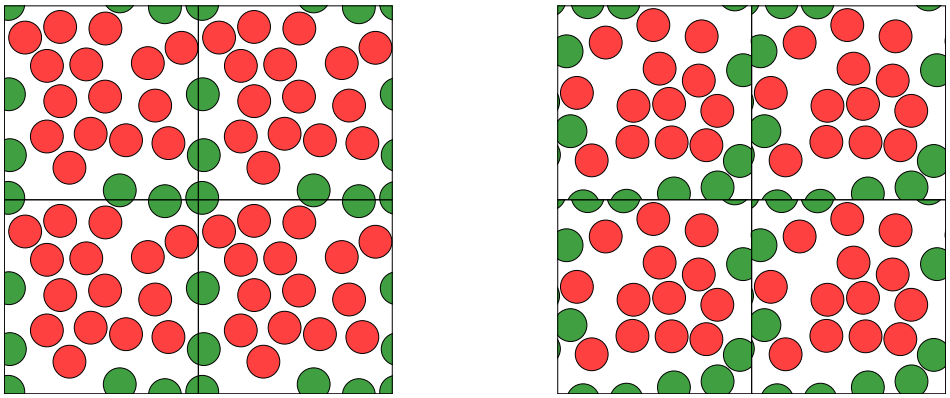

(a) Realization of a periodized ensemble (b) Realization of a snapshot

Figure 1: Periodic versus snapshot ensembles, one realization periodically extended, particles intersecting the cell boundary highlighted in green

was reported [17]. Classical RVE studies of stochastic models of microstructures [18–20], often referred to as microstructure generators, report both the bias and the dispersion to assess the representativity of the generated structures. However, the serious problems associated with snapshot microstructures – the primary state in which experimental samples are provided – have only recently been recognized [13]. Moreover, we wish to emphasize that mitigation strategies for reducing the bias were introduced and analyzed in the community of mathematical analysis only. Indeed, there are only a few microstructure models which are amenable to a rigorous mathematical treatment like random checkerboards or Gaussian random fields. Computational investigations were then conducted mostly to verify the theoretical predictions. In contrast, microstructure models in continuum micromechanics and materials science are typically not treatable analytically, and it is by no means clear that phenomena observed in "academic" cases play a role in applied scenarios, and whether proposed mitigations work as expected. As an example, there are only a few studies [15, 16] that report on the magnitude of the bias for snapshot ensembles of realistic materials, e.g., matrix-inclusion composites at industrial volume fractions.

1.3 Strategies for reducing the bias

In the following, we focus on this setting of non-periodic microstructures and discuss approaches to control the associated bias that were proposed in the mathematical community. There are actually two general strategies. The first approach is based on modifying the governing equation – the balance of linear momentum in linear elasticity – with an additional zero-order ("massive") term which was proposed and analyzed in the context of stochastic homogenization [8, 10, 21] and computational multiscale schemes [22–24]. These approaches link the slow decrease of the bias to the decay rate of the Green's function for conductivity (and linear elasticity): The disturbances introduced at the cell boundary of a snapshot microstructure pollute the solution field on the entire cell. As a mitigation, the equation to solve is changed such that the associated Green's function has a faster, typically exponential, decay in space. From a physical point of view, this approach may be interpreted as changing from a static model - with infinite propagation speed - to a dynamic model that has a finite speed of wave propagation. Due to this limited spreading rate of information, for a suitably chosen time, an interior part of the cell remains unaffected by anything that happens on the cell boundary. While effective in theory, these methods require modifications of the underlying equations and solver implementations. Therefore, these approaches were analyzed and tested for academic examples and in the setting of conductivity only. To the best of

our knowledge, there is no application of these ideas to realistic microstructures and linear elasticity.
An alternative approach proceeds by filtering the solution field or, equivalently, by discarding a boundary layer, originally proposed for periodic homogenization problems [25–28], where the evaluation of apparent properties is restricted to an interior subdomain. This so-called subsample averaging strategy is based on the idea that considering a larger domain for solving the underlying PDE naturally supplies boundary conditions for the subsampled domain, thereby reducing boundary layer effects. Recent theoretical results [29] established that this approach can improve the convergence rate of the bias in stochastic homogenization problems [30] as well, at least in the conductivity setting and for ensembles that can be treated by mathematical analysis. However, its practical performance for elasticity problems and realistic microstructures, as well as its interaction with the dispersion, remain largely unexplored. Moreover, restricting the evaluation to a smaller interior domain reduces the available sampling volume, which leads to an increase in the dispersion. Thus, subsample averaging introduces a trade-off between reducing bias and increasing dispersion. This trade-off is directly related to the size of the subsample averaging domain,

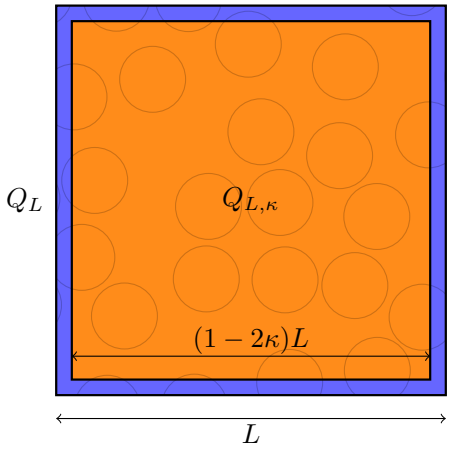

Figure 2: Subsample averaging domain $Q_{L,\kappa}$ inside the unit cell Q_L.

illustrated in Fig. 2.

1.4 FFT-based computational micromechanics

Classical computational homogenization is most commonly performed using finite element methods (FEM) [31–33], which are flexible with respect to geometry and boundary conditions and were widely applied in multiscale simulations. Over the last decades, however, FFT-based computational micromechanics, originally introduced by Moulinec and Suquet [34,35], emerged as an efficient alternative for unit cell computations [36,37]. By exploiting the convolution structure of the underlying equations and aided by the superconvergence of averaged stresses [38–40], FFT-based methods enable simulations at very large resolutions, making them particularly attractive for image-based microstructures and industrial-scale problems [41–43]. The relative advantages and limitations of FEM- and FFT-based approaches were investigated in a number of comparative studies [44–46], highlighting differences in accuracy, computational efficiency, and the treatment of boundary conditions [47–49]. We wish to stress, however, that FFT-based computational homogenization methods enabled the analysis of the bias and the dispersion associated with the RVE method for realistic and industrially relevant microstructures at large scale. This property is highly attractive for understanding the properties of microstructure ensembles and error mitigation strategies in stochastic homogenization.

1.5 Outline

Previous numerical studies showed that for elastic composites, the bias in snapshot microstructures can be comparable in magnitude to the dispersion, making its control essential [16]. In this work, we provide a comprehensive computational study of subsample averaging for elasticity problems on realistic microstructures, more precisely matrix-inclusion composites with elastic fillers inside a polymer matrix. While previous works established theoretical improvements for conductivity problems and idealized settings, its practical performance for large-scale elastic simulations and such industrially relevant microstructures has not been systematically assessed.
The present study closes this gap through the following contributions:

- We show that subsample averaging must be applied consistently to both stress and strain fields; subsample averaging the apparent stress alone may reduce the magnitude of the bias, but does not improve its convergence rate.
- We identify a bias–dispersion trade-off: subsample averaging reduces bias but increases dispersion, leading to only marginal improvement of the total error when used in isolation.
- We demonstrate that combining subsample averaging with variance reduction [50–53] via optimized volume fraction significantly improves accuracy and reliability.

We particularly emphasize the first point: Subsample averaging targets minimizing boundary effects by discarding data on a boundary zone. However, when applied naively to the apparent stress only, it does not improve the convergence rate of the bias. From a micromechanical perspective, such an approach is inconsistent with the Hill-Mandel macrohomogeneity condition [1, 54]. Subsample averaging both the apparent strain and stress fields, i.e., the choice guided by the Hill-Mandel condition, leads to the desired improvement.

2 Bias, dispersion and subsample averaging

In this section, we briefly recall the decomposition of the stochastic homogenization error into bias and dispersion and introduce the subsample averaging approach, which is central to the subsequent analysis. We consider the set of stiffness distributions

$$\mathcal{C} = \left\{ \mathbb{C} : \mathbb{R}^d \to L(\mathrm{Sym}(d)) \,\middle|\, \alpha_- \|\boldsymbol{\varepsilon}\|^2 \leq \boldsymbol{\varepsilon} \,:\, \mathbb{C}(\boldsymbol{x}) : \boldsymbol{\varepsilon} \leq \alpha_+ \|\boldsymbol{\varepsilon}\|^2, \quad \boldsymbol{\varepsilon} \in \mathrm{Sym}(d), \quad \boldsymbol{x} \in \mathbb{R}^d \right\} \tag{2.1}$$

in d spatial dimensions, with strains $\boldsymbol{\varepsilon}$ as well as positive constants $\alpha_\pm$ and where $\mathrm{Sym}(d)$ denotes the vector space of symmetric second-order tensors. As it originates from an elastic stored energy, the stiffness tensor $\mathbb{C}$ is represented by a fourth-order tensor which has both major and minor symmetries. The central ingredient of stochastic homogenization [55, 56] is a given probability distribution μ on the set of stiffness tensors (2.1) which is assumed to be stationary and ergodic. The effective stiffness $\mathbb{C}^{\mathrm{eff}}$ serves as the primary output quantity, and emerges from solutions of the corrector equation which is however posed on the full space $\mathbb{R}^d$ rendering it computationally intractable.
We seek to approximate the effective stiffness $\mathbb{C}^{\mathrm{eff}}$ by computing the apparent stiffness $\mathbb{C}_L^{\mathrm{app}}$ of a microstructure realization of the ensemble on the cubic cell

$$Q_L = [0, L]^d. \tag{2.2}$$

The apparent stiffness $\mathbb{C}_L^{\mathrm{app}}$ is obtained by first solving the balance of linear momentum for the displacement fluctuation $\boldsymbol{u}_L$

$$\mathrm{div}\,(\mathbb{C} : (\bar{\boldsymbol{\varepsilon}} + \nabla^{\mathrm{s}} \boldsymbol{u}_L)) = \boldsymbol{0}. \tag{2.3}$$

Here, the displacement fluctuation $\boldsymbol{u}_L$ is sought in the space $H^1_{\#}(Q_L)^d$, comprised of square-integrable periodic vector fields which have a weak derivative that is also square-integrable. In eq. (2.3), ∇^{s} denotes the symmetric gradient and the microstructure realization is encoded by the stiffness distribution $\mathbb{C}$. The balance of linear momentum (2.3) is subject to a macroscopic strain $\bar{\boldsymbol{\varepsilon}}$ and periodic boundary conditions for the displacement fluctuations and antiperiodicity conditions for the normal stresses

$$\boldsymbol{u}_L \ \#, \qquad (\mathbb{C} : (\bar{\boldsymbol{\varepsilon}} + \nabla^{\mathrm{s}} \boldsymbol{u}_L)) \cdot \boldsymbol{n} - \ \# \tag{2.4}$$

on the boundary of the cubic cell (2.2). The apparent stiffness itself is then implicitly defined by the Hill-Mandel macrohomogeneity condition [1, 54]

$$\mathbb{C}^{\mathrm{app}}_L : \fint_{Q_L} \bar{\boldsymbol{\varepsilon}} + \nabla^{\mathrm{s}} \boldsymbol{u}_L \ \mathrm{d}V = \fint_{Q_L} \mathbb{C} : (\bar{\boldsymbol{\varepsilon}} + \nabla^{\mathrm{s}} \boldsymbol{u}_L) \ \mathrm{d}V \tag{2.5}$$

for varying imposed strain $\bar{\boldsymbol{\varepsilon}} \in \mathrm{Sym}(d)$. Here, the slash stands for the mean-value integral. As the displacement fluctuation $\boldsymbol{u}_L$ is periodic, the average of the associated symmetrized gradient vanishes. In particular, we may express the left hand side of eq. (2.5) in the form

$$\fint_{Q_L} \bar{\boldsymbol{\varepsilon}} + \nabla^{\mathrm{s}} \boldsymbol{u}_L \ \mathrm{d}V = \bar{\boldsymbol{\varepsilon}}. \tag{2.6}$$

The apparent properties converge to the effective properties in the volume limit [57, 58]

$$\lim_{L \to \infty} \mathbb{C}^{\mathrm{app}}_L = \mathbb{C}^{\mathrm{eff}} \tag{2.7}$$

almost surely. However, it is generally more practical to compute a number of apparent stiffnesses on cells of the same size and determine the effective stiffness by taking the mean of these samples [11].
The deviation of an apparent stiffness $\mathbb{C}^{\mathrm{app}}_L$ from the effective stiffness $\mathbb{C}^{\mathrm{eff}}$ – the correct value – decomposes naturally into two distinct parts. Using the ensemble mean,

$$\langle \mathbb{C} \rangle = \int_{\mathcal{C}} \mathbb{C} \ d\mu(\mathbb{C}), \tag{2.8}$$

of the probability measure μ of the set (2.1) of stiffness distributions, the total deviation decomposes as follows [8, 11]

$$\langle \| \mathbb{C}^{\mathrm{eff}} - \mathbb{C}^{\mathrm{app}}_L \|^2 \rangle = \| \mathbb{C}^{\mathrm{eff}} - \langle \mathbb{C}^{\mathrm{app}}_L \rangle \|^2 + \langle \| \langle \mathbb{C}^{\mathrm{app}}_L \rangle - \mathbb{C}^{\mathrm{app}}_L \|^2 \rangle, \tag{2.9}$$

involving the bias, also called *systematic error*,

$$\mathfrak{E}_{\mathrm{bias}} = \| \mathbb{C}^{\mathrm{eff}} - \langle \mathbb{C}^{\mathrm{app}}_L \rangle \|, \tag{2.10}$$

and the dispersion

$$\mathfrak{E}_{\mathrm{disp}} = \sqrt{\langle \| \langle \mathbb{C}^{\mathrm{app}}_L \rangle - \mathbb{C}^{\mathrm{app}}_L \|^2 \rangle}. \tag{2.11}$$

The bias (2.10) quantifies the deviation of the mean apparent stiffness on a fixed cell size from the effective stiffness. The dispersion (2.11) measures the fluctuation of the apparent stiffness on a fixed cell size.
Both parts of the total deviation decrease as the length L of the cubic cell Q_L is increased, at least for large cell sizes. However, they do so at different rates, and their magnitude depends on the problem under consideration. For conductivity, the bias turns out to be negligible for some industrial-scale composites [15]. However, an investigation [16] of the linear elastic behavior of the same materials revealed that the bias is much larger in that case. Furthermore, the effective stiffness is not known, as otherwise no numerical or experimental study would be necessary to determine it.
If long-range correlations are absent, the dispersion (2.11) decays with the rate

$$\mathfrak{E}_{\mathrm{disp}} \lesssim L^{-\frac{d}{2}} \tag{2.12}$$

of the central limit theorem (CLT) [59]. In other words, the dispersion shows the same behavior as the local average

$$\langle \mathbb{C}_L \rangle = \fint_{Q_L} \mathbb{C} \, \mathrm{d}V, \tag{2.13}$$

although the apparent stiffness $\mathbb{C}_L^{\mathrm{app}}$ defined in eq. (2.5) involves the solution of the PDE (2.3), i.e., corresponds to some kind of *non-local* average. An inferior rate is observed for materials with long-range correlations, e.g., infinitely long fibers [60, 61].

The decay rate of the bias (2.10) was observed to depend on whether a suitably periodized ensemble is used or not [13, 62]. We distinguish between *periodized* (PER) ensembles and *snapshots* (CUT).

In both cases, the displacement fluctuation $\boldsymbol{u}_L$ is subject to periodic boundary conditions (2.4). However, only for periodized ensembles, the geometric construction of the microstructure obeys periodic boundary conditions. To illustrate, Fig. 1 shows realizations of a periodized and a snapshot ensemble of randomly placed non-overlapping circular inclusions with uniform radius, where inclusions intersecting the cell boundary are highlighted in green. In both cases, the realization is extended periodically in both the x- and y-direction, as encoded by the periodic boundary conditions (2.4) enforced while solving the balance of linear momentum (2.3). For the periodized ensemble, illustrated in Fig. 1(a), inclusions intersecting the cell boundary are periodically extended, whereas this is not the case for snapshot realizations, see Fig. 1(b).

For periodized ensembles, the bias (2.10) typically decays with the rate

$$\mathfrak{E}_{\mathrm{bias}} \lesssim L^{-d}. \tag{2.14}$$

However, for snapshots, the expected rate of decay [13]

$$\mathfrak{E}_{\mathrm{bias}} \lesssim L^{-1} \tag{2.15}$$

is worse, not only compared to periodized ensembles (2.14), but also compared to the dispersion (2.12) when working in three dimensions (and higher). Recently [16], computational experiments in linear elasticity reported behavior compatible with the scaling (2.15) for a class of microstructures of engineering relevance. It was also shown that the inferior decay rate of the bias (2.15) seriously increases the computational effort necessary compared to periodized ensembles to determine the effective properties to a similar degree of accuracy.

Acquiring apparent properties with this method (2.5) leads to the aforementioned decay rates (2.12), (2.14) and (2.15). However, we need to clarify a fundamental mismatch between the theoretical analysis and the engineering practice. The latter is more concerned with the absolute deviations of the apparent stiffness and the errors introduced by working on cells of finite size. The decay rates are less interesting because, on the one hand, computational facilities are limited, and, on the other hand, the decay behavior may just emerge beyond accuracy levels required for engineering practice. Unfortunately, from the viewpoint of mathematical analysis, obtaining rigorous results on the decay rates is conceptually simpler than deriving results on the involved prefactors.

In this work, we follow a hybrid approach. We investigate both the bias and the dispersion on cells of varying size and monitor both the magnitude and the decay rate if possible. Of course, obtaining an accurate estimate of the decay rate may be infeasible in case the magnitude of the quantities is too small.

As a possible mitigation of the inferior convergence behavior of the snapshot bias (2.15), a classical approach called oversampling solves the PDE (2.3) on a larger domain and extracts the apparent properties on a subzone only [25]. More recently, a more intrusive strategy was investigated: The underlying PDE (2.3) is augmented by an additional zero-order ("massive") term [8, 10, 21], see also the works [22–24]. These methods, although provably successful, require changing the numerical solver, and, in particular,

the implementation. Moreover, in linear elasticity, adding a zero-order term to the balance of linear momentum has no direct physical interpretation.

Recently, theoretical results [29] hinted at the superiority of a comparatively simple strategy. Taking a solution $\boldsymbol{u}_L$ of the PDE (2.3), instead of taking the average on the entire cell (2.2) in eq. (2.5), the averages are calculated on a specific subvolume

$$Q_{L,\kappa} = [\kappa L, (1-\kappa)L]^d, \qquad 0 < \kappa < \frac{1}{2}, \tag{2.16}$$

only, illustrated in Fig. 2. The κ-subsampled apparent stiffness $\mathbb{C}^{\text{app}}_{L,\kappa}$ is defined by the relation

$$\mathbb{C}^{\text{app}}_{L,\kappa} : \fint_{Q_{L,\kappa}} \bar{\boldsymbol{\varepsilon}} + \nabla^{\text{s}} \boldsymbol{u}_L \, \mathrm{d}V = \fint_{Q_{L,\kappa}} \mathbb{C} : (\bar{\boldsymbol{\varepsilon}} + \nabla^{\text{s}} \boldsymbol{u}_L) \, \mathrm{d}V. \tag{2.17}$$

Note that, in contrast to the case without subsample averaging (2.6), the average of the gradient of the displacement fluctuation $\boldsymbol{u}_L$ of the subsampled domain (2.16) need not vanish,

$$\fint_{Q_{L,\kappa}} \nabla^{\text{s}} \boldsymbol{u}_L \, \mathrm{d}V \neq \boldsymbol{0}, \tag{2.18}$$

in general. However, it was also shown [29] that ignoring the fact (2.18) and obtaining the apparent stiffness via

$$\widetilde{\mathbb{C}}^{\text{app}}_{L,\kappa} : \bar{\boldsymbol{\varepsilon}} = \fint_{Q_{L,\kappa}} \mathbb{C} : (\bar{\boldsymbol{\varepsilon}} + \nabla^{\text{s}} \boldsymbol{u}_L) \, \mathrm{d}V \tag{2.19}$$

does improve the magnitude of the bias for snapshots, but the convergence rate (2.15) *remains unchanged.* This observation reveals that subsample averaging **must be applied consistently to both stress and strain fields**; restricting the averaging to the stress alone does not improve the convergence rate of the bias.

Subsample averaging reduces boundary-induced errors by restricting the evaluation to an interior domain. However, this reduction in domain size decreases the available sampling volume, which increases the dispersion, leading to a bias–dispersion trade-off. More explicitly, as the subsampled domain (2.16) is necessarily smaller than the original domain Q_L, the dispersion (2.12) is expected to increase, as the edge length of the subsampled region

$$L_\kappa = (1 - 2\kappa)L \tag{2.20}$$

is smaller than the edge length L.

A series expansion of the effective stiffness tensor of an infinitely large two-phase isotropic composite $\mathbb{C}^{\text{eff}}$, see Milton [63, §14],

$$\mathbb{C}^{\text{eff}} = \langle \mathbb{C} \rangle + O((\sqrt{k}-1)/(\sqrt{k}+1)) = \mathbb{C}_1 + \phi \, (\mathbb{C}_2 - \mathbb{C}_1) + O((\sqrt{k}-1)/(\sqrt{k}+1)) \tag{2.21}$$

where ϕ denotes the inclusion volume fraction, $\mathbb{C}_1$ and $\mathbb{C}_2$ denote the stiffness tensors of the matrix and inclusion phases, respectively, and k denotes the material contrast. Equation (2.21) applies to the effective properties of an infinite medium and does not provide a quantitative description of the apparent properties of the finite domains considered here. We use it only as a heuristic motivation for expecting fluctuations in volume fraction to influence apparent properties. The magnitude of this influence for the finite domains and subsamples studied here is determined directly from the numerical experiments. To reduce the deviations, it is therefore advantageous to consider samples with a volume fraction that is close to that of the material under investigation [15, 16].

This observation motivates the use of variance reduction techniques, such as optimized volume fraction, which is combined with subsample averaging in the subsequent sections.

3 Methods

3.1 Outline

In this section, we describe the generation of microstructures and the numerical methods used to systematically investigate the interplay between bias and dispersion introduced in Section 2.

3.2 Microstructure generation

Microstructures with spherical inclusions are generated using the mechanical contraction method (MCM) [64], which produces random packings at prescribed volume fractions. Fiber-reinforced microstructures are generated using the sequential addition and migration (SAM) algorithm [43], which allows prescribing orientation distributions via the fiber orientation tensor. For the convenience of the reader, the used algorithms are summarized in Apx. A. It is important to note that these generation algorithms yield *analytic*, i.e., not yet discretized, representations of the objects occupying the microstructure.

The generated microstructures are discretized by voxels (volume pixels), where each voxel is assigned to either the matrix or the inclusion depending on the location of its center. Fig. 3 shows the analytical representation of a two-dimensional snapshot with circular inclusions, which is discretized onto a 100^2 *pixel* grid, shown in Fig. 3(b). To generate a snapshot, a periodic microstructure of twice the edge length of the cubic cell (2.2) is generated first. The snapshot realization is then taken as the central part with dimensions of the cubic cell (2.2) of that aforementioned larger microstructure.

In the discrete setting, the volume fractions (A.1) and (A.6) may not be realized exactly for three different reasons. First, for monodisperse fibers, the volume fraction can only be an integer multiple of the volume fraction of a microstructure with a single fiber. Second, snapshots may further deviate from the prescribed volume fraction as the part outside the cell of a particle intersecting the boundary is not present on the opposing side. Third, there may be a deviation inferred by the discretization on a voxel grid.

As discussed in the previous section, matching the macroscopic volume fraction of a composite increases the probability of a microstructure sample to yield an accurate apparent property. To make this insight actionable, Le Bris et al. [50] proposed a selection approach for variance reduction: Only those samples with sufficiently accurate volume fraction are retained. Fischer [65] proved that such an approach does indeed yield a bias-free variance-reduction method.

Unfortunately, discarding samples comes with a significant computational overhead. A simple alternative was proposed by Ravichandran et al. [16] in case an analytic description of the composite microstructure is available: the optimized volume fraction (OVF) procedure [16]. It uses a Newton-type method to iteratively rescale the particle sizes to match the originally prescribed volume fraction. The centroids $\boldsymbol{x}_i$ and, in case of fibers, orientations $\boldsymbol{p}_i$ are not modified, meaning the OVF procedure takes place after the SAM/MCM algorithm is finished.

After generating the discrete microstructure, the discrete volume fraction ϕ_k of the inclusion phase at step k

$$\phi_k = \frac{N_{\mathrm{vx},p}}{N_{\Sigma\mathrm{vx}}} \tag{3.1}$$

with the number of voxels $N_{\mathrm{vx},p}$ assigned to the inclusion phase and the total number of voxels $N_{\Sigma\mathrm{vx}}$ is calculated. A uniform rescaling factor c for all inclusions is introduced, i.e., for spheres the radius

$$\tilde{r} = c\, r \tag{3.2}$$

and for fibers both the diameter and length

$$\tilde{d} = c\, d \tag{3.3}$$

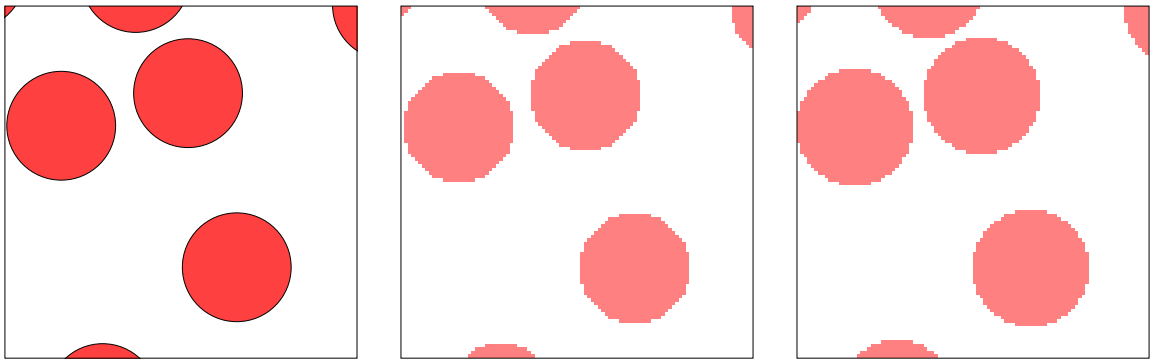

(a) Analytical representation, area fraction $\phi = 25.158\%$

(b) Discretized, area fraction $\phi_0 = 25.72\%$

(c) OVF procedure yields area fraction of $\phi_2 = 29.71\%$

Figure 3: OVF procedure applied to a two-dimensional microstructure snapshot discretized onto a 100^2 pixel grid, target area fraction $\phi = 30\%$

$$\tilde{\ell} = c\,\ell \tag{3.4}$$

are rescaled. Both for spheres and fibers, this results in the volume fraction (A.1), (A.6) being rescaled

$$\tilde{\phi}_{\text{sph}} = c^3 \phi_{\text{sph}} \tag{3.5}$$

$$\tilde{\phi}_{\text{fib}} = c^3 \phi_{\text{fib}} \tag{3.6}$$

by the same prefactor. The rescaling factor c has to be chosen such that a volume fraction ϕ_0 matches the target volume fraction ϕ, i.e.,

$$\Phi(c) = \phi - c^3 \phi_0 \stackrel{!}{=} 0. \tag{3.7}$$

Using Newton's method to find roots of the objective function (3.7), an iterative procedure for c is obtained as

$$c_{k+1} = c_k - \frac{c_k^3 \phi_0 - \phi}{3 c_k^2 \phi_0}, \tag{3.8}$$

which can be rewritten as

$$\frac{c_{k+1}}{c_k} = 1 + \frac{\phi - c_k^3 \phi_0}{3 c_k^3 \phi_0}. \tag{3.9}$$

Considering the relations (3.5) and (3.6), the volume fraction at iteration k is

$$\phi_k = c_k^3 \phi_0. \tag{3.10}$$

Inserting the discrete volume fraction (3.10) into the rescaling prefactor equation (3.9) yields the relation

$$\frac{c_{k+1}}{c_k} = 1 + \frac{\phi - \phi_k}{3\phi_k}. \tag{3.11}$$

Thus, if a deviation beyond an acceptable tolerance from the originally prescribed volume fraction ϕ is present, the diameters d and possibly lengths ℓ of all particles are iteratively rescaled by the prefactor (3.11).

The discrete microstructure is then generated again by assigning a phase to a voxel depending on which phase contains the center of that voxel. The procedure is repeated until the tolerance is satisfied or no significant improvement is observed, as the volume fraction can only at most be approximated by discrete steps of the inverse of the total number of voxels

$$|\Delta\phi_{k,\min}| = \frac{1}{N_{\Sigma\text{vx}}}. \tag{3.12}$$

Fig. 3 shows the OVF procedure applied to a two-dimensional microstructure with circular inclusions. The grid chosen for discretization is 100^2 *pixels* in size. The initial *area* fraction deviates from the target area fraction by more than four percent, shown in Fig. 3(b). After three iterations, the area fraction deviates from the target by less than one percent, shown in Fig. 3(c), while the discretized microstructure does not appear to look much different.

The OVF procedure optimizes the volume fraction in the domain used to evaluate the discrete volume fraction (3.10). Thus, the volume fraction can be either optimized to be exact over the whole cubic cell (2.2) or the subsample averaging domain (2.16).

3.3 Solving the problem with FFT-based methods

FFT-based computational micromechanics [36] utilizes that a strain field $\boldsymbol{\varepsilon}_L = \bar{\boldsymbol{\varepsilon}} + \nabla^{\mathrm{s}} \boldsymbol{u}_L$ solving the balance of linear momentum (2.3) equivalently solves the Lippmann-Schwinger equation

$$\boldsymbol{\varepsilon}_L = \bar{\boldsymbol{\varepsilon}} - \mathbb{\Gamma}^0 : \delta\mathbb{C} : \boldsymbol{\varepsilon}_L \tag{3.13}$$

with the stiffness polarization $\delta\mathbb{C} = \mathbb{C} - \mathbb{C}_0$ and the Eshelby-Green operator $\mathbb{\Gamma}^0 = \nabla^{\mathrm{s}} G^0 \mathrm{div}$. Originally, the Lippmann-Schwinger equation (3.13) directly served as an iterative scheme [34], using the right-hand side to define the subsequent iterate

$$\boldsymbol{\varepsilon}_L^{k+1} = \bar{\boldsymbol{\varepsilon}} - \mathbb{\Gamma}^0 : \delta\mathbb{C} : \boldsymbol{\varepsilon}_L^k. \tag{3.14}$$

However, faster methods for solving the Lippmann-Schwinger equation (3.13), such as the conjugate gradient method (CG) [66] were introduced. For the nonlinear case, solvers such as Newton's method [67,68] and nonlinear CG [69] are available. While CG and Newton's method require more memory, using a Barzilai-Borwein adapted step size [70] yields similar performance gains compared to the so-called "basic scheme" (3.14) for simple material behaviors without substantially increased memory requirements.

In this work, we solve the balance of linear momentum (2.3) using the conjugate gradient method (CG), as it is linear and a workstation with sufficient memory is available to the authors. The staggered grid discretization [71] is employed, a discretization which leads to considerably fewer artifacts than the original discretization introduced by Moulinec and Suquet [34, 35]. Moreover, the influence of voxelization artifacts on the computed apparent stiffness is mitigated by the superconvergence of averaged stresses in computational homogenization [40].

The Lippmann-Schwinger equation (3.13) is solved to a relative tolerance of 10^{-9}. To do so, a workstation with 192 CPU cores and 1 Terabyte of memory is employed. The CG method uses four strain fields. Each field stores six components per voxel, as the strain is a symmetric second-order tensor. Each component is stored as a double precision floating point number and thus occupies eight bytes of memory. As such, to solve a problem of $32^3 = 32768$ voxels, six Megabytes of memory are necessary, whereas the reference computation of 1024^3 voxels requires 192 Gigabytes of memory. Problems of the size 32^3 are solved in at most one to five seconds, whereas the runtime for a problem of 1024^3 voxels is on the order of multiple hours.

3.4 Quantifying the bias and the dispersion

A number of N microstructure samples are generated yielding a list of (scalar) apparent Young's moduli $E_{\mathrm{i}}^{\mathrm{app}}$, see Appendix B. We compute the mean

$$\mu_{\mathrm{E}} = \frac{1}{N} \sum_{i=1}^{N} E_{\mathrm{i}}^{\mathrm{app}} \tag{3.15}$$

and sample variance

$$\mathrm{Var_E} = \frac{1}{N-1}\sum_{i=1}^{N}(E_\mathrm{i}^\mathrm{app} - \mu_\mathrm{E})^2 \tag{3.16}$$

with the standard deviation defined as its root

$$\sigma_\mathrm{E} = \sqrt{\mathrm{Var_E}}. \tag{3.17}$$

In the work at hand, to quantify the bias, the mean (3.15) of the apparent stiffness of ten periodized microstructures 1024^3 voxels in size is used as a proxy for the effective modulus E^eff. If the effective stiffness $\mathbb{C}^\mathrm{eff}$ is not known, assessing that the bias is suitably low can be determined by increasing the size of the cubic cell Q_L and verifying that the mean of the apparent stiffness $\langle \mathbb{C}_L^\mathrm{app} \rangle$ shows sufficiently small deviation.

We compute the relative dispersion

$$\mathfrak{e}_\mathrm{disp} = \frac{\sigma_\mathrm{E}}{E^\mathrm{eff}}, \tag{3.18}$$

and the relative bias

$$\mathfrak{e}_\mathrm{bias} = \frac{|\mu_\mathrm{E} - E^\mathrm{eff}|}{E^\mathrm{eff}}. \tag{3.19}$$

As an alternative measure of the statistical uncertainty of the estimated ensemble mean, one may consider the relative 95% confidence-interval half-width

$$\mathfrak{e}_\mathrm{ci,95\%} = \frac{1.96\,\sigma_\mathrm{E}}{\sqrt{N}\,E^\mathrm{eff}}. \tag{3.20}$$

For a fixed number N of realizations, the confidence-interval half-width (3.20) differs from the relative dispersion (3.18) by the factor $1.96/\sqrt{N}$. In the present study, however, the number of realizations varies with the cell size. Therefore, the confidence-interval half-width and the relative dispersion need not exhibit identical scaling across all resolutions. We use the relative dispersion (3.18) as our primary visualization metric because it characterizes the variability of the apparent properties of individual realizations. The confidence-interval half-width (3.20), by contrast, quantifies the statistical uncertainty of the estimated ensemble mean.

As an engineering benchmark, we compute the probability of being within a margin of the effective value E^eff by counting for how many realizations the apparent property $E_\mathrm{i}^\mathrm{app}$ lies within the specified range of the effective property E^eff

$$|E_\mathrm{i}^\mathrm{app} - E^\mathrm{eff}| < b\ E^\mathrm{eff}, \tag{3.21}$$

and dividing by the total number of realizations N. The parameter b is set as $b = 0.01$ and $b = 0.001$, corresponding to being within 1% and 0.1% of the effective modulus, respectively.

4 Results

4.1 Setup

The following results consistently demonstrate the bias–dispersion trade-off introduced by subsample averaging: while the bias is reduced, the dispersion increases due to the reduced sampling domain.

We consider generated microstructures made of two phases, which both have linear elastic and isotropic material behavior. The material parameters are listed in Tab. 1, taken from Hessman et al. [72], who investigated fiber-reinforced plastic microstructures commonly used in industry.

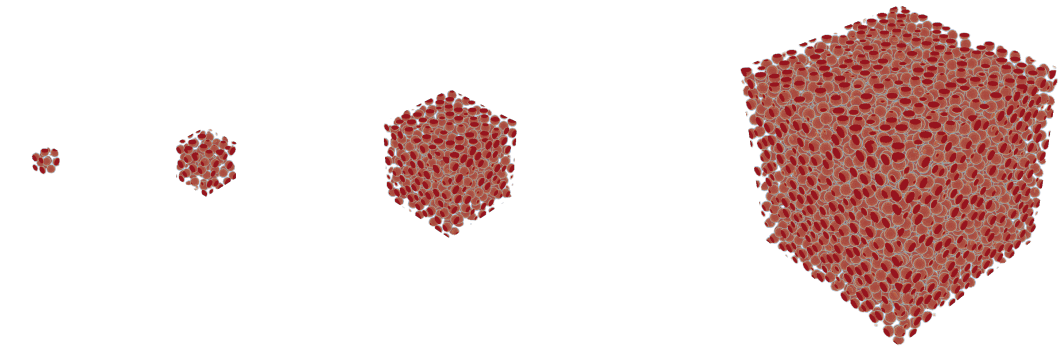

(a) 32^3 (b) 64^3 (c) 128^3 (d) 256^3

Figure 4: Non-overlapping spheres, showcase of different microstructure realizations

	Material	Young's modulus	Poisson's ratio
Matrix	polyamide-66	3 GPa	0.4
Inclusion	E-Glass	72 GPa	0.22

Table 1: Material parameters

To investigate the magnitude of both the bias and the dispersion discussed in section 2, microstructures of increasing size were generated, with the number of inclusions proportional to the microstructure size. The microstructures are discretized by 32^3, 64^3, 128^3 and 256^3 voxels. The values for the subsample averaging parameter κ introduced in equation (2.16) are chosen such that the voxels discarded scale with the increase in microstructure size. The largest degree of subsample averaging investigated is $\kappa = 0.25$. At the value $\kappa = 0.25$, the subsample averaging interval (2.20) is reduced to half of its original length and thus the volume is reduced to an eighth of its original value.

κ	0	0.03125	0.0625	0.09375	0.125	0.15625	0.1875	0.21875	0.25
32	[0, 32]	[1, 31]	[2, 30]	[3, 29]	[4, 28]	[5, 27]	[6, 26]	[7, 25]	[8, 24]
64	[0, 64]	[2, 62]	[4, 60]	[6, 58]	[8, 56]	[10, 54]	[12, 52]	[14, 50]	[16, 48]
128	[0, 128]	[4, 124]	[8, 120]	[12, 116]	[16, 112]	[20, 108]	[24, 104]	[28, 100]	[32, 96]
256	[0, 256]	[8, 248]	[16, 240]	[24, 232]	[32, 224]	[40, 216]	[48, 208]	[56, 200]	[64, 192]

Table 2: Subsample averaging masks

The specific values investigated and the corresponding subsample averaging domains are listed in Tab. 2. For the 32^3 and 64^3 resolutions, 3000 samples were generated. For the 128^3 resolution, 1000 samples were generated, and 500 samples were generated for the 256^3 resolution.

4.2 Spherical inclusions

We consider composites with spherical inclusions at a volume fraction of 30%. The inclusion diameter is chosen such that there are sixteen voxels per sphere diameter, following the accuracy recommendations in related work [15, 16]. In the periodic case, for $K \in \{2, 4, 8, 16\}$, the number of spheres is $N_{\text{sph}} = K^3$. The microstructure edge length is $L = 16K\ell_{\text{vx}}$, with the voxel edge length ℓ_{vx} chosen to be 1 µm. With

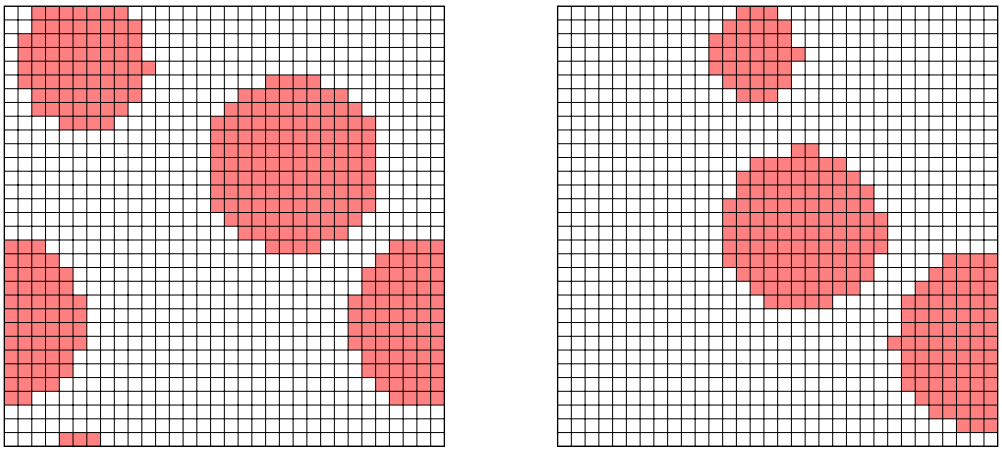

(a) Slice through discretized, periodic non-overlapping spheres, 32^3, $\phi = 30.11\%$

(b) Slice through discretized, non-periodic non-overlapping spheres, 32^3, $\phi = 25.78\%$

Figure 5: Periodic versus snapshot realization for a size of 32^3 voxels, target volume fraction $\phi = 30\%$

the volume fraction specified via

$$\phi = \frac{N\pi d_{\text{sphere}}^3}{6L^3} = \frac{K^3\pi d_{\text{sphere}}^3}{6 \cdot 16^3 K^3 \ \ell_{\text{vx}}^3} = \frac{\pi d_{\text{sphere}}^3}{6 \cdot 16^3 \ \ell_{\text{vx}}^3}, \tag{4.1}$$

the diameter of the inclusions is constrained

$$d_{\text{sphere}} = 16 \sqrt[3]{\frac{6\phi}{\pi}} \ \ell_{\text{vx}}, \tag{4.2}$$

and must be $d_{\text{sphere}} = 13.289$ µm for the case at hand. A minimum distance of $0.2 \cdot d_{\text{sphere}}$ is enforced in the microstructure generation algorithm (A.2). Fig. 4 shows microstructure realizations for the four resolutions from Tab. 2, where the voxel edge length ℓ_{vx} is held constant.

Fig. 5 shows a slice through a periodic and a snapshot microstructure realization discretized with 32^3 voxels. The discretized structure matches the volume fraction of 30% set during the microstructure generation. However, the snapshot microstructure without optimized volume fraction only has a realized volume fraction of 26%.

As the material behavior of the matrix and the inclusion is isotropic, and the spheres are randomly distributed, we expect the material behavior of the composite to be isotropic as well. Therefore, we investigate the Young's modulus E of the isotropic projection of the apparent stiffness only. For the computation of the scalar Young's modulus E from a fourth-order stiffness tensor $\mathbb{C}$, we refer to Appendix B.

The following results consistently illustrate the bias–dispersion trade-off introduced by subsample averaging: while the bias is reduced, the dispersion increases due to the reduced sampling domain.

The different values of the subsampling parameter κ applied to sampling the apparent stiffness (2.19), (2.17), outlined in table 2, are represented in this manuscript by a color gradient from black, representing no subsampling, $\kappa = 0$, via blue to lime, representing the highest volume reduction by a factor of eight, $\kappa = 0.25$.

Subsample averaging both stress and strain reduces the magnitude of the bias and produces a more favorable decay trend for snapshots (Fig. 6). While subsample averaging the apparent stress without subsample averaging the strain (2.19) does decrease the magnitude of the bias as seen in Fig. 6(b), subsample averaging both stress and strain (2.17) yields much better results as seen in Fig. 6(a). Without

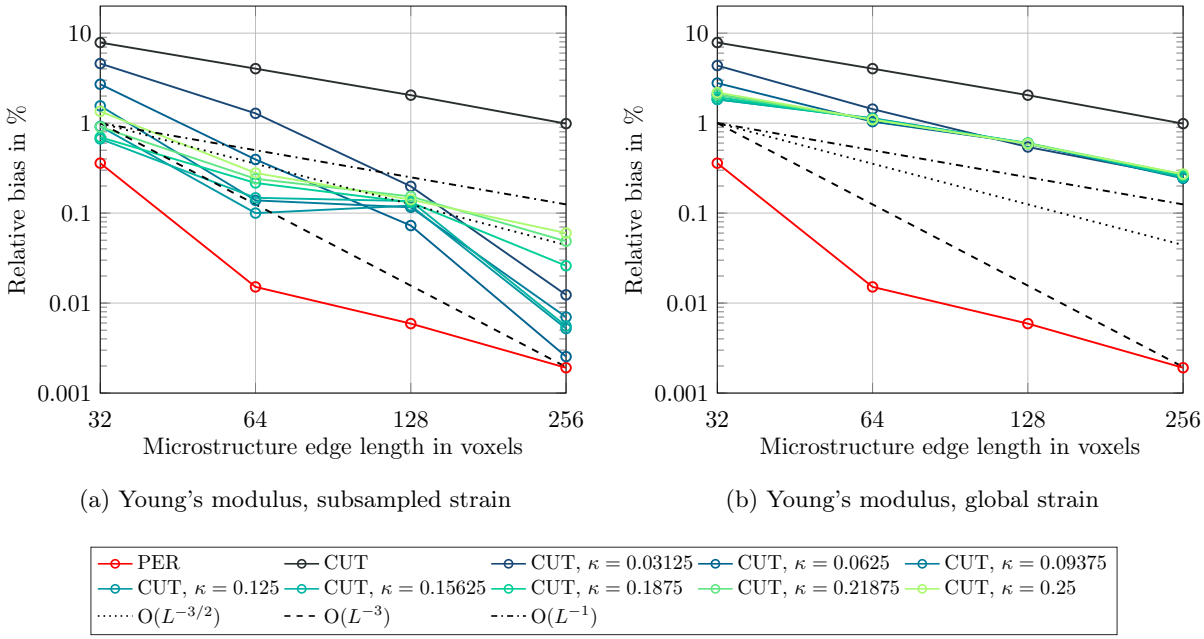

(a) Young's modulus, subsampled strain

(b) Young's modulus, global strain

Figure 6: Bias for periodic (PER) and snapshot ensembles (CUT) with spherical fillers, no OVF

subsample averaging the strain, any degree of subsample averaging results in the same bias reduction, whereas with subsampled strain, differences become apparent: Whereas for an edge length of 64 voxels, the lowest bias is observed for $\kappa = 0.125$, cyan, at 256 voxels, the lowest bias is observed for $\kappa = 0.0625$, dark blue. A **key observation** is that **subsample averaging the apparent stress alone does not improve** the convergence rate of the bias, whereas subsample averaging **both** stress and strain leads to a **more favorable decay trend**.

The bias for periodized ensembles is consistent with the expected L^{-3} decay (2.14). Without subsample averaging the strain (2.19), see Fig. 6(b) the bias for snapshots with subsample averaging is lower in magnitude than for snapshots and no subsample averaging, but appears broadly consistent with the same L^{-1} decay (2.15) typical for snapshots. With subsample averaging the strain (2.17), shown in Fig. 6(a), the bias for snapshots exhibits a trend that is more consistent with an $L^{-3/2}$ decay, with the larger values of the subsampling parameter κ appearing closer to an L^{-3} decay for higher values of the subsample averaging parameter κ (2.16).

Subsample averaging increases the dispersion due to the reduced averaging domain, while optimized volume fraction (see section 3) substantially lowers its magnitude (Fig. 7). As shown in Fig. 7(a), even without OVF, as subsample averaging is increased, the dispersion also increases as the size of the volume used for effective property computation is decreased, as seen by the greener curves signifying more subsampling situated above the dark-blue curves signifying less subsampling. With OVF, as shown in Fig. 7(b), although the dispersion is lower without subsample averaging, as the subsample averaging parameter κ (2.16) is increased, visualized via a color gradient from dark blue to lime, the effect of the optimized volume fraction decreases: The OVF procedure enforces the correct volume fraction over the entire cell, not in the subsampled region. As such, while the correct volume fraction is guaranteed for no subsample averaging, this is not the case once subsample averaging is performed. As the subsample averaging mask is increased, the dispersion for OVF approaches the magnitude of the dispersion without OVF. In contrast, the bias is largely unaffected by the optimized volume fraction, indicating that OVF primarily targets random fluctuations rather than bias, as visible in Fig. 7(c) and Fig. 7(d). The OVF

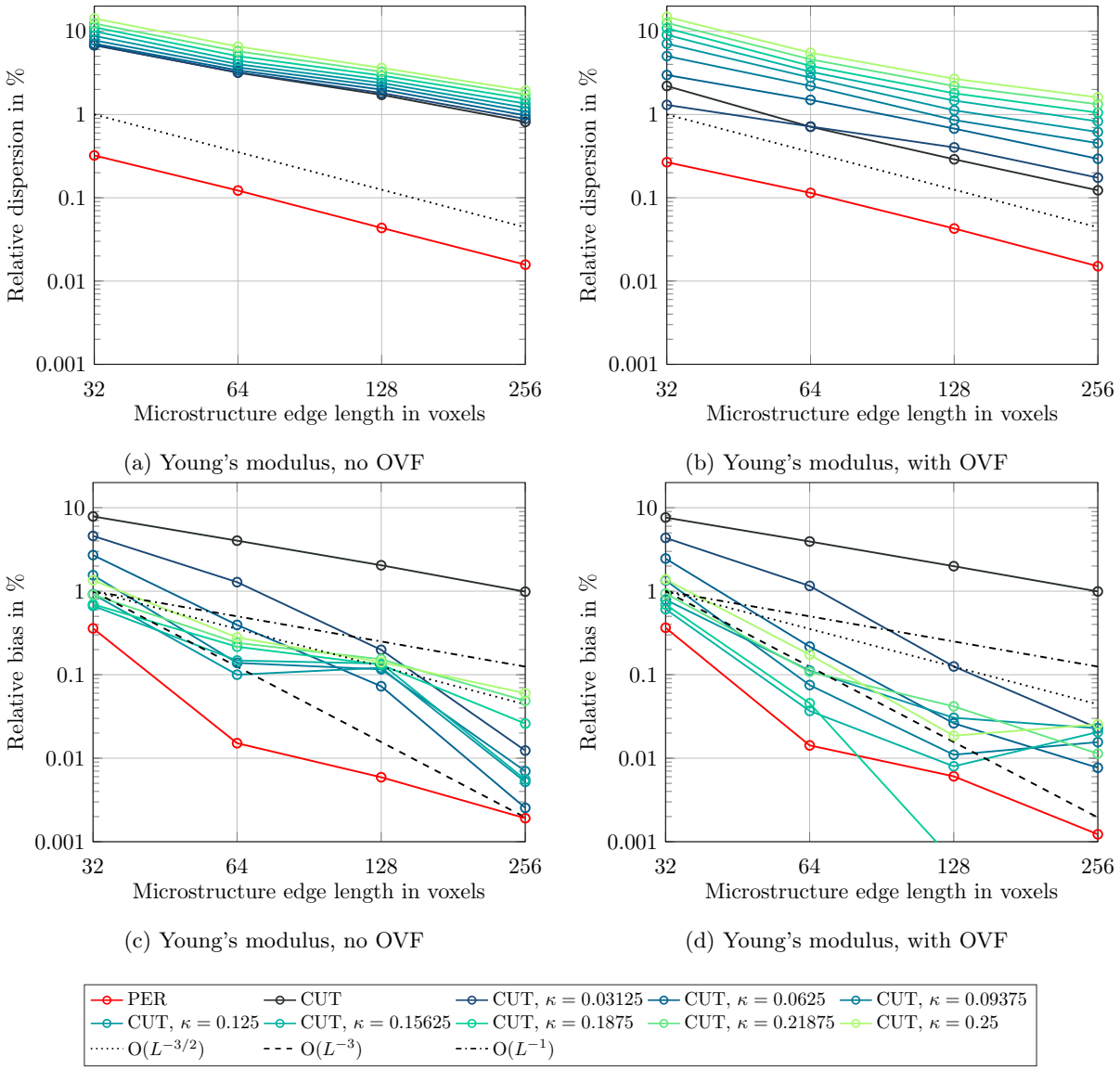

(a) Young's modulus, no OVF

(b) Young's modulus, with OVF

(c) Young's modulus, no OVF

(d) Young's modulus, with OVF

Figure 7: Bias and dispersion for periodic (PER) and snapshot ensembles (CUT) with spherical fillers

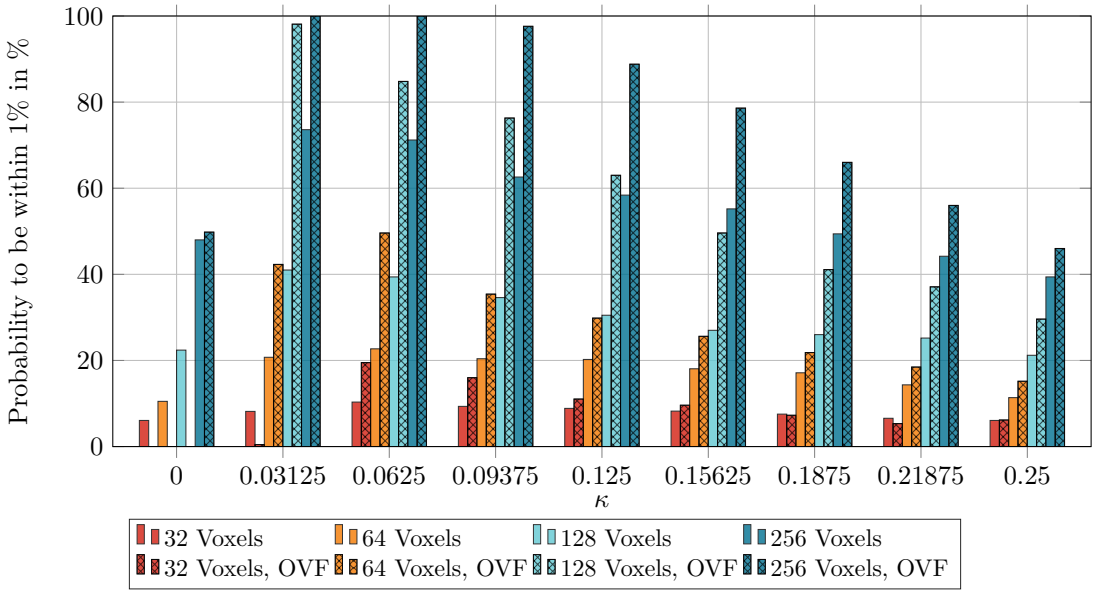

Figure 8: Spherical inclusions: empirical probability of a snapshot result being within 1% of E^{eff}

procedure therefore allows for a decrease in dispersion, thus **reducing the variance while not affecting the bias**.

To interpret the practical impact of the competing error contributions, we evaluate the probability of obtaining effective properties within a prescribed tolerance. Combining subsample averaging with optimized volume fraction significantly increases the probability of obtaining apparent properties close to the effective value (Fig. 8). The performance of snapshots without subsample averaging compared to periodized microstructures is inferior. While periodized ensembles at the lowest resolution of 32^3 voxels yield a 97.8% probability of being within 1% of the effective property, snapshots achieve this feature only 49.8% of the time at the highest resolution of 256^3 voxels. Without subsample averaging, optimized volume fraction decreases the probability of being close to the effective Young's modulus, as previously observed [16]. This behavior is a consequence of the bias–dispersion decomposition (2.9): If the bias dominates, reducing the variance alone does not improve the total error, but instead makes realizations cluster more tightly around a biased mean. As a result, the probability of being close to the true effective value may decrease despite a reduction in variance. Only if the bias is first reduced, for example through subsample averaging, does variance reduction become beneficial.

Indeed, if subsample averaging is used, the lower bias increases the probability of success, and the lower dispersion resulting from the optimized volume fraction further aids in being closer to the effective Young's modulus, by a factor of roughly two. There is a sweet spot: Beyond subsample averaging with $\kappa = 0.0625$, the increasing dispersion results in higher total error, even though the bias is still decreasing.

Tab. 3 shows the likelihood of being close to the effective properties when enforcing the volume fraction to be exact on the **same** domain as the subsample averaging instead of the whole domain (2.2). OVF was enforced on the domains that provided the most promising results for OVF over the whole domain. The improvement for $\kappa = 0.03125$ subsample averaging is only marginal, for 64 voxels, the results are actually slightly worse. However, at $\kappa = 0.0625$ subsample averaging, the 128^3 voxel resolution has a 99.7% probability of being within 1% of the correct Young's modulus compared to 84.8% before, and the 64 voxel resolution has a 89.1% probability compared to the previous 49.6%. These findings show that while it is potentially beneficial to perform volume fraction optimization on the same domain as

Table 3: Empirical success probability to be Δ-close to E^{eff}, spherical inclusions

			OVF for $Q_{L,\kappa}$		OVF for Q_L		no OVF	
	κ	Len.	1%-close	0.1%-close	1%-close	0.1%-close	1%-close	0.1%-close
PER	/	32	99.13 %	11.18 %	99.13 %	11.18%	97.56 %	13.08 %
		64	100.00 %	62.30 %	100.00 %	62.30 %	100.00 %	57.73 %
		128	100.00 %	97.60 %	100.00 %	97.60 %	100.00 %	97.10 %
		256	100.00 %	100.00 %	100.00 %	100.00 %	100.00 %	100.00 %
CUT	0.00000	32	0.00 %	0.00 %	0.00 %	0.00 %	6.07 %	0.73 %
		64	0.00 %	0.00 %	0.00 %	0.00 %	10.50 %	1.37 %
		128	0.00 %	0.00 %	0.00 %	0.00 %	22.40 %	3.00 %
		256	49.80 %	0.00 %	49.80 %	0.00 %	48.00 %	6.20 %
CUT	0.03125	32	1.30 %	0.07 %	0.47 %	0.07 %	8.17 %	0.77 %
		64	39.87 %	0.50 %	42.30 %	3.53 %	20.73 %	1.97 %
		128	99.90 %	30.80 %	98.10 %	20.70 %	41.00 %	4.50 %
		256	100.00 %	55.40 %	100.00 %	43.80 %	73.60 %	8.00 %
CUT	0.06250	32	16.93 %	1.23 %	19.50 %	1.80 %	10.33 %	0.70 %
		64	89.10 %	14.57 %	49.60 %	4.77 %	22.70 %	2.13 %
		128	99.70 %	26.80 %	84.80 %	12.40 %	39.40 %	3.20 %
		256	100.00 %	56.40 %	100.00 %	24.80 %	71.20 %	7.40 %

subsampling, it is **not** required to substantially improve accuracy.

4.3 Fiber-reinforced microstructures

We consider fiber microstructures with a volume fraction of 15%, inspired by studies conducted on scans of real microstructures [72, 73]. The fibers were chosen to have an aspect ratio ℓ/d of 20, with the length $\ell = 64$ µm. The fibers have the same length as the microstructure edge length for 64 voxels and the number of inclusions is on the same order of magnitude as for the spherical inclusions in section 4.2. For the 64^3-voxel microstructures, the number of inclusions is 76 fibers. The number of voxels per fiber was shown to be sufficient in related work [15, 16]. A minimum distance of $0.2 \cdot d_{\text{fiber}}$ is enforced in the microstructure generation algorithm. To generate isotropic fiber microstructures, the second-order fiber

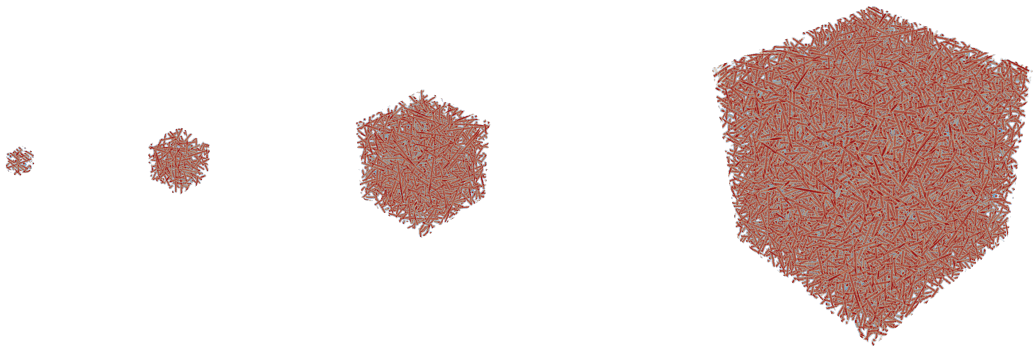

(a) 32^3 (b) 64^3 (c) 128^3 (d) 256^3

Figure 9: Non-overlapping isotropic fibers, showcase of different microstructure realizations

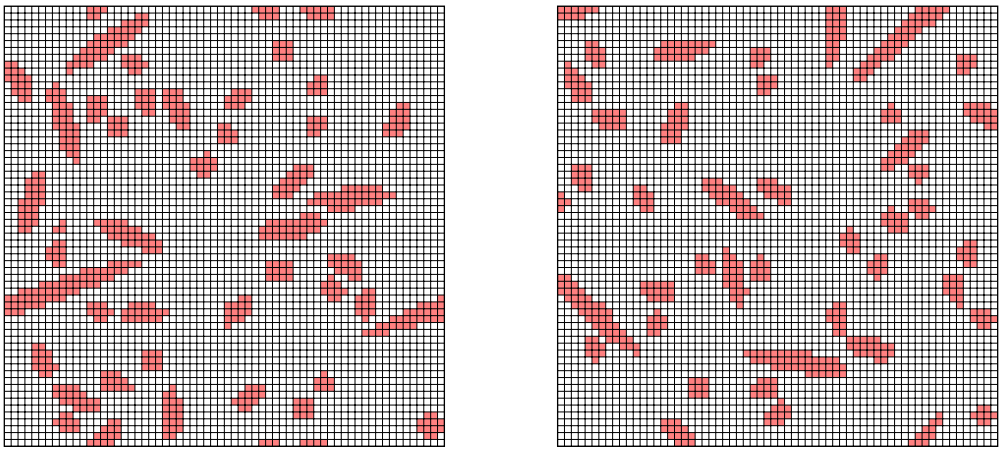

(a) Slice through discretized, periodic non-overlapping fibers, 64^3, $\phi = 15.01\%$

(b) Slice through discretized, non-periodic non-overlapping fibers, 64^3, $\phi = 14.75\%$

Figure 10: Periodic versus snapshot ensembles for size 64^3 voxels, target volume fraction $\phi = 15\%$

orientation tensor [74, 75] is set to

$$\boldsymbol{A}_{\text{iso}} = \begin{bmatrix} 1/3 & 0 & 0 \\ 0 & 1/3 & 0 \\ 0 & 0 & 1/3 \end{bmatrix}. \tag{4.3}$$

To generate transversely isotropic microstructures, we choose

$$\boldsymbol{A}_{\text{trans}} = \begin{bmatrix} 0.8 & 0 & 0 \\ 0 & 0.1 & 0 \\ 0 & 0 & 0.1 \end{bmatrix}. \tag{4.4}$$

For orthotropic microstructures, we use

$$\boldsymbol{A}_{\text{ortho}} = \begin{bmatrix} 0.5 & 0 & 0 \\ 0 & 0.4 & 0 \\ 0 & 0 & 0.1 \end{bmatrix}. \tag{4.5}$$

Fig. 9 shows microstructure realizations for the resolutions specified in table 2. The number of voxels per fiber is kept the same. Therefore, a higher resolution corresponds to increasing the RVE candidate size and thus the number of fibers.

Fig. 10 shows a slice of sampled fiber microstructures with isotropic orientation (4.3) discretized by 64^3 voxels without optimized volume fraction. In Fig. 10(a), a fiber intersecting the unit cell boundary on the lower half of the left wraps around to the right. For the snapshot, shown in Fig. 10(b), a fiber intersecting the unit cell boundary on the lower left does not have a corresponding fiber on the opposite side. The volume fraction of the snapshot realization deviates further from the volume fraction supplied to the microstructure generation algorithm compared to the periodized ensemble.

For fiber-reinforced microstructures, we observe similar trends as for spherical inclusions: Subsample averaging both stress and strain reduces the bias, whereas subsample averaging the apparent stress only does not improve its convergence behavior (Fig. 11). In detail, Fig. 11(b) shows the relative bias (3.19) for subsample averaging the apparent stress, but not the strain (2.19) for fiber-reinforced microstructures with isotropic orientation (4.3). For snapshots, the observed trend is broadly consistent with L^{-1} behavior,

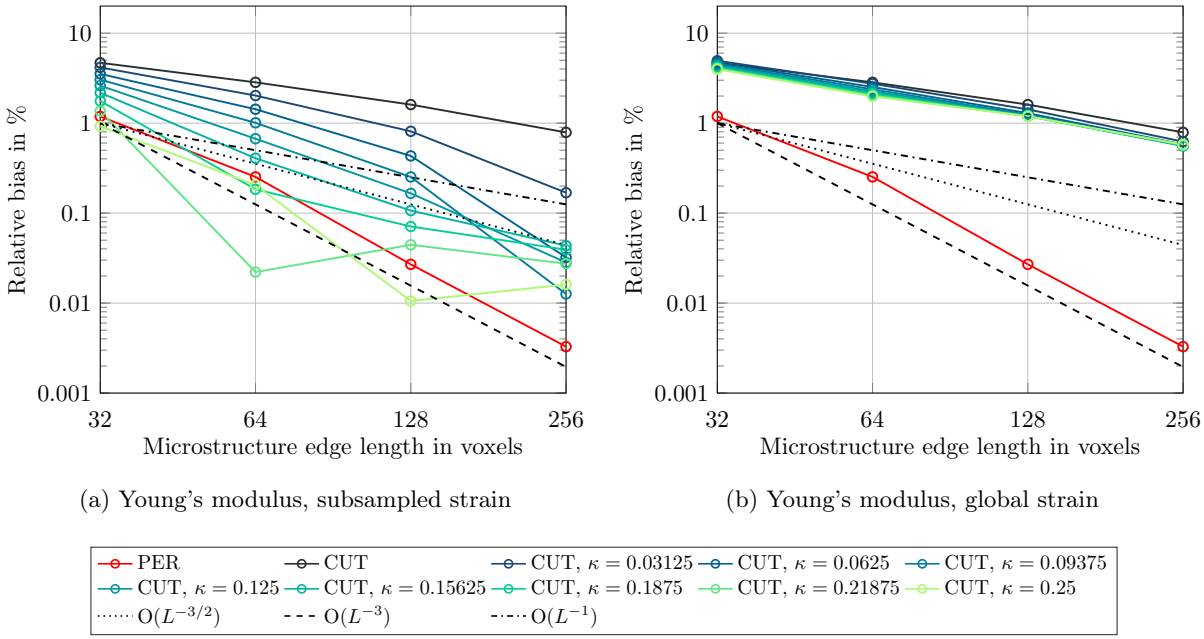

(a) Young's modulus, subsampled strain

(b) Young's modulus, global strain

Figure 11: Bias for periodic (PER) and snapshot ensembles (CUT) for fiber reinforced microstructures with isotropic orientation (4.3), no OVF

whereas the bias for periodized ensembles is consistent with the expected L^{-3} decay (2.14). Unlike for spherical inclusions, recall Fig. 6(b), a significant reduction in magnitude of the bias is not observed, and varying the size of the subsample averaging domain (2.16) denoted by the parameter κ does not significantly influence the results. Fig. 11(a) shows the relative bias for subsample averaging both stress and strain (2.17). A reduction in magnitude is observed, and the observed trend is more consistent with an $L^{-3/2}$ decay than without subsample averaging. The bias is influenced by the size of the subsample averaging domain (2.16), signified by a color progression from dark blue to lime, with a larger subsample averaging mask (2.16) generally leading to a lower bias.

The bias–dispersion trade-off persists for fiber-reinforced microstructures: Increasing the degree of subsample averaging, signified by a color progression from dark blue to lime, reduces the bias but leads to higher dispersion. Fig. 12 shows the relative dispersion (3.18) and the relative bias (3.19) for fibers with isotropic orientation (4.3). The dispersion, both without optimizing the volume fraction (3.11), shown in Fig. 12(a), or with optimizing the volume fraction, shown in Fig. 12(b), is broadly consistent with an $L^{-3/2}$ decay (2.12). The dispersion for snapshots is larger in magnitude than for periodized ensembles, and an increase of the subsample averaging parameter κ, see eq. (2.16), further increases the dispersion. Optimized volume fraction decreases the dispersion, but this effect diminishes as the subsample averaging parameter is increased. The bias, shown without OVF in Fig. 12(c) and with OVF in Fig. 12(d) is not influenced significantly by OVF. Apparently, compared to spherical inclusions, shown in Fig. 7, the individual subsampled results differ more strongly from each other.

Subsample averaging combined with optimized volume fraction substantially improves the probability of obtaining accurate effective properties for snapshot microstructures. Figure 13 shows that optimized volume fraction combined with subsample averaging increases the probability of being close to the effective property with snapshots significantly. To be within 1% of the effective value, with periodized ensembles, a resolution of 64^3 voxels is sufficient. With snapshots of the same resolution, the apparent property is only 1%-close with a probability of 40.33%, using a subsample averaging mask (2.16) of $\kappa = 0.09375$ and

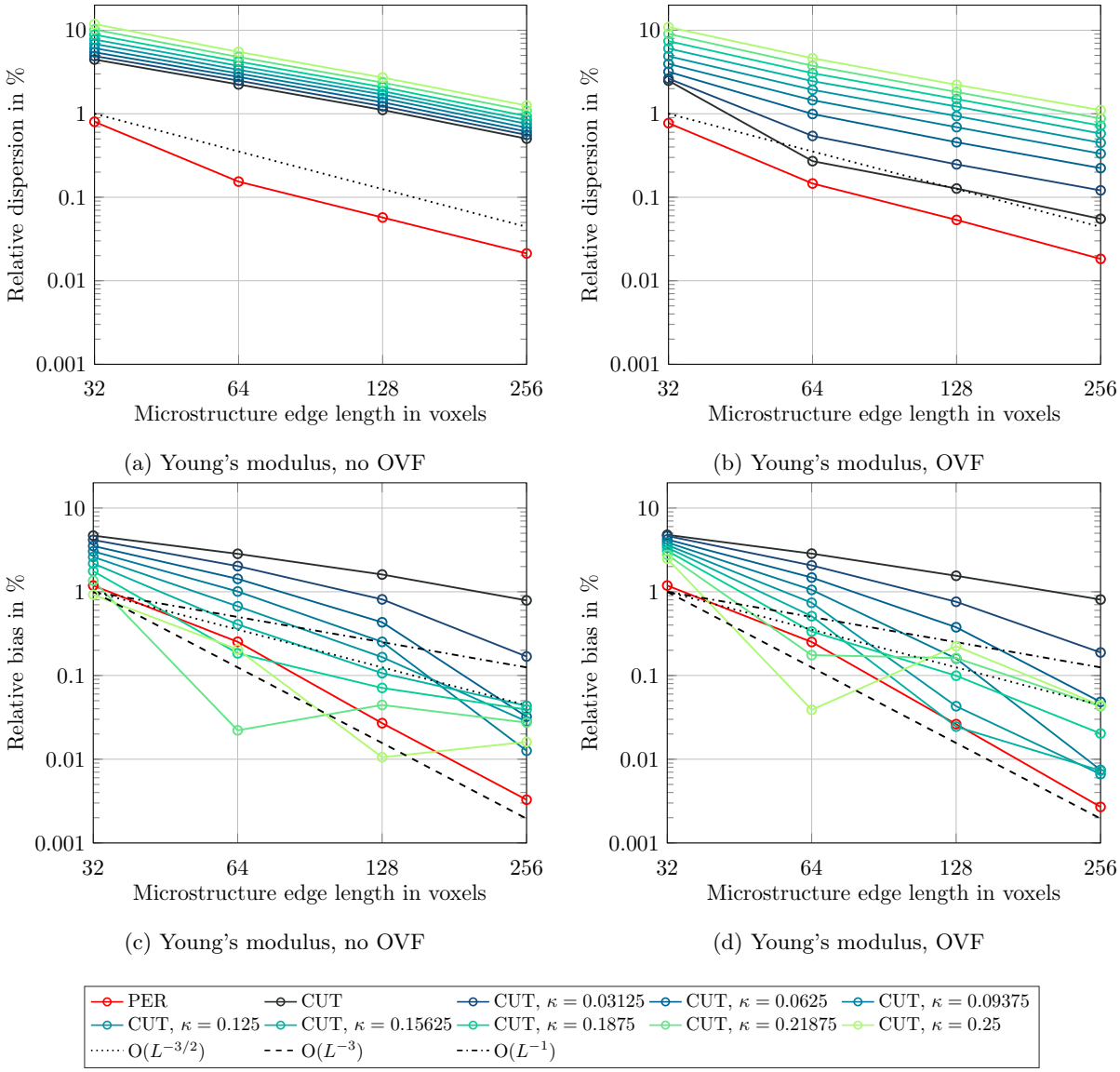

(a) Young's modulus, no OVF

(b) Young's modulus, OVF

(c) Young's modulus, no OVF

(d) Young's modulus, OVF

Figure 12: Bias and dispersion for periodic (PER) and snapshot ensembles (CUT) for fiber reinforced microstructures with isotropic orientation (4.3)

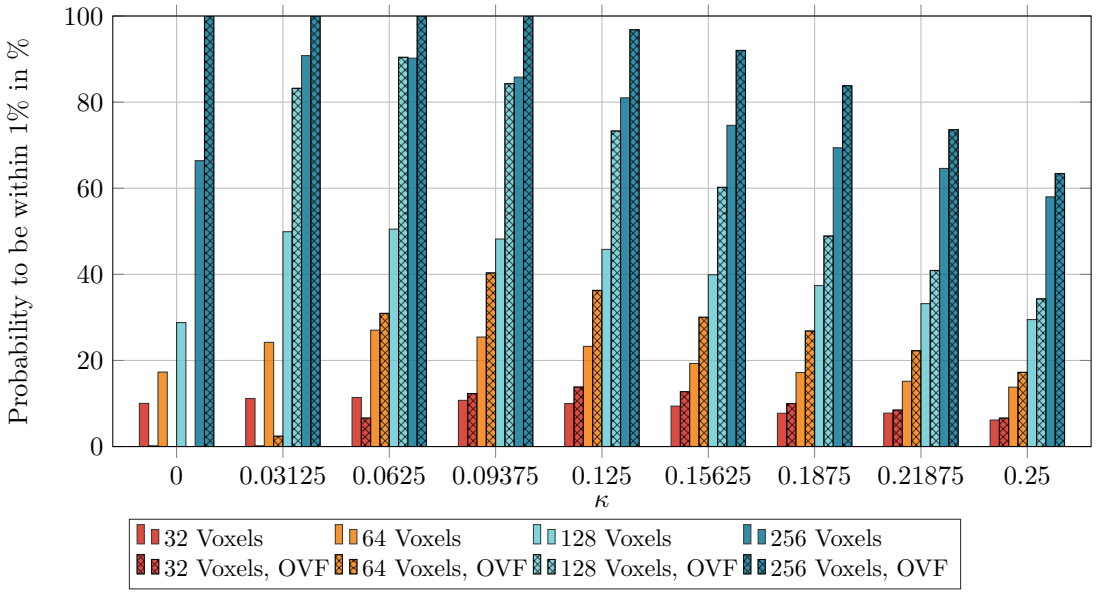

Figure 13: Fibers with isotropic orientation (4.3), snapshots, probability of being within 1% of E^{eff}

optimized volume fraction. Increasing the computational effort by a factor of eight by using 128^3 voxels yields a 90.4% success rate with $\kappa = 0.0625$, which is much better than the success rate of 28.8% with no subsample averaging at all. A 100% rate of success can only be achieved by doubling the edge length once again to 256^3 voxels, which works both for subsample averaging and no subsample averaging at all ($\kappa = 0$).

Table 4 shows enforcing the volume fraction in the subsampled domain for a subsample averaging mask of $\kappa = 0.0625$ instead of the whole domain. The domain of the averaging mask $\kappa = 0.0625$ was chosen as it previously showed the most accurate results. The probability of being within 1% of the effective Young's modulus for 128^3 voxels increases from 90.4% to 100%, however, for 64^3 voxels, it decreases from 30.93% to 9.03%. As for the spherical inclusions, these findings yield an interesting conclusion: While performing subsampling and OVF on the same domain may be beneficial, it is **not necessary** for the two techniques to yield substantial improvements in accuracy. In particular, these techniques may be employed independently of each other. From a practical viewpoint, this characteristic feature turns out to be rather advantageous: OVF is a *preprocessing* step performed on the microstructures on which the balance of linear momentum (2.3) is solved, whereas subsample averaging is a *postprocessing* step applied to the obtained solution field.

For fibers with the transversely isotropic orientation (4.4), we consider the longitudinal Young's modulus E_{LL} as the material property of interest, which corresponds to the principal direction associated with the largest component of the second-order FOT (4.4). The detailed procedure for computing the longitudinal Young's modulus E_{LL} from the apparent stiffness of a realization is outlined in Appendix B. The relative bias for snapshots without optimized volume fraction shown in Fig. 14(c), is lower than the relative bias for periodized ensembles at higher values of the subsample averaging parameter κ , signified by a color progression from dark blue to lime. With optimized volume fraction enabled, shown in Fig. 14(d), this effect is less pronounced. The relative bias for snapshots without subsample averaging is broadly consistent with an L^{-1} decay (2.15), while the relative bias for periodized microstructures is consistent with an L^{-3} decay (2.14) at resolutions of 64^3 voxels and higher.

The success rate of being close to the effective properties, shown in Tab. 7, does not benefit from the

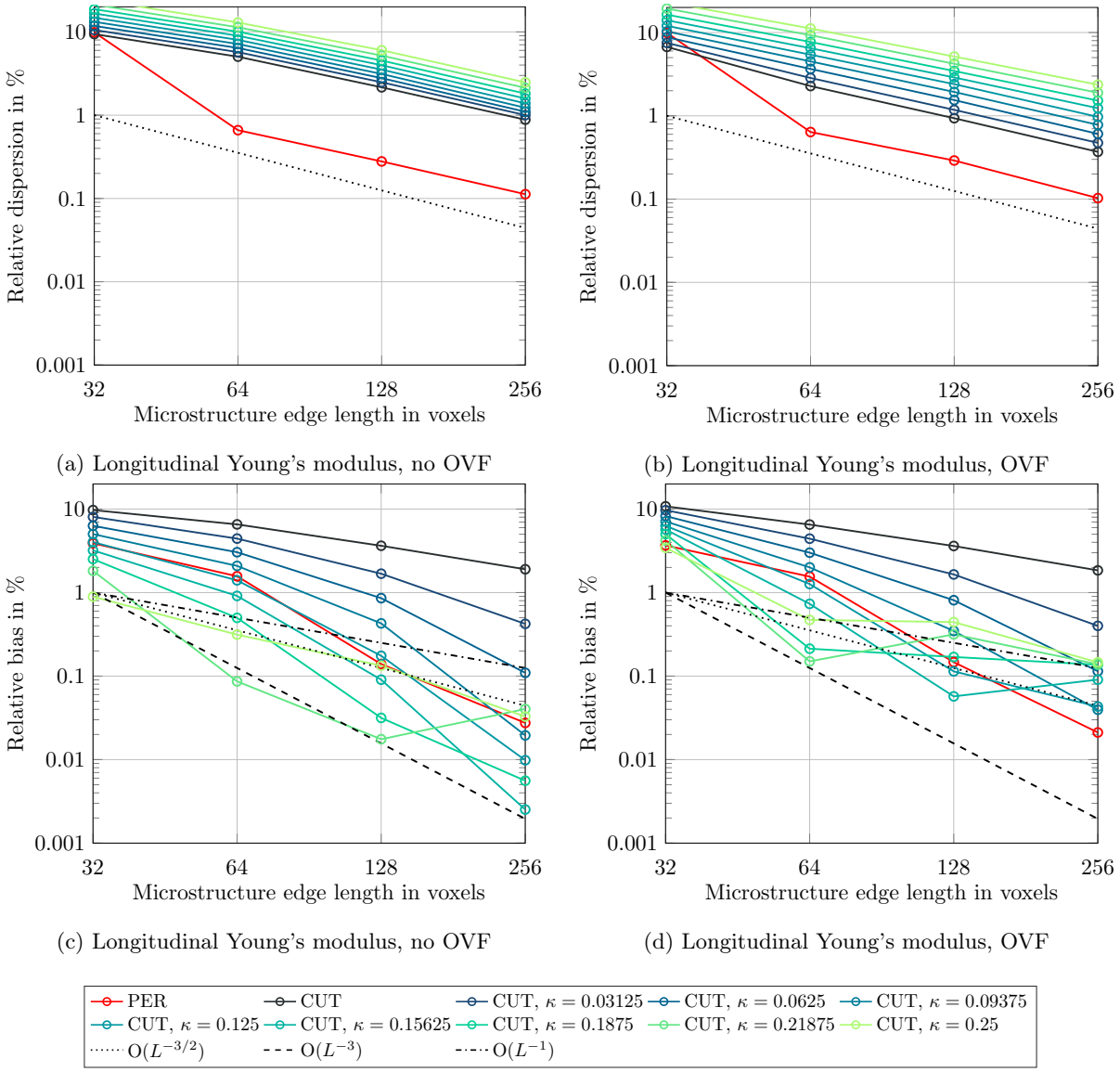

(a) Longitudinal Young's modulus, no OVF

(b) Longitudinal Young's modulus, OVF

(c) Longitudinal Young's modulus, no OVF

(d) Longitudinal Young's modulus, OVF

Figure 14: Bias and dispersion for periodic (PER) and snapshot ensembles (CUT) for fibers with transversely isotropic orientation (4.4)

Table 4: Empirical success probability to be Δ-close to E^{eff}, fibers with isotropic orientation (4.3)

			OVF for $Q_{L,\kappa}$		OVF for Q_L		no OVF	
	κ	Len.	1%-close	0.1%-close	1%-close	0.1%-close	1%-close	0.1%-close
PER	/	32	42.37 %	3.40 %	42.37 %	3.40 %	43.39 %	3.78 %
		64	100.00 %	14.83 %	100.00 %	14.83 %	100.00 %	15.43 %
		128	100.00 %	91.00 %	100.00 %	91.00 %	100.00 %	88.80 %
		256	100.00 %	100.00 %	100.00 %	100.00 %	100.00 %	100.00 %
CUT	0.0000	32	0.12 %	0.00 %	0.12 %	0.00 %	10.03 %	1.20 %
		64	0.00 %	0.00 %	0.00 %	0.00 %	17.30 %	1.63 %
		128	0.00 %	0.00 %	0.00 %	0.00 %	28.80 %	1.50 %
		256	100.00 %	0.00 %	100.00 %	0.00 %	66.40 %	4.80 %
CUT	0.0625	32	0.61 %	0.06 %	6.61 %	0.90 %	11.40 %	1.17 %
		64	9.03 %	0.13 %	30.93 %	2.70 %	27.03 %	2.40 %
		128	100.00 %	4.70 %	90.40 %	12.60 %	50.50 %	7.20 %
		256	100.00 %	73.40 %	100.00 %	35.80 %	90.20 %	11.60 %

lower bias compared to periodized ensembles, as the dispersion, shown in Fig. 14(a), and Fig. 14(b), is higher. Optimizing the volume fraction leads to a decrease in dispersion, although this effect is less pronounced than for fibers with isotropic orientation (4.3), shown in Fig. 12(b). As the size of the subsample averaging domain (2.16) is increased, the variance reduction due to the OVF procedure is decreased. Still, optimized volume fraction with subsample averaging provides better results compared to just using subsample averaging by itself. Being within 1% of the effective properties with 256^3 voxels and subsample averaging is possible with a 90% probability, whereas 128^3 voxels suffice in the periodic setting. However, these success rates are significantly better than using no subsample averaging, so from the perspective of possibly having only snapshot microstructures to work with, subsample averaging proves to be helpful.

For fibers with the orthotropic orientation (4.5), we consider the largest Young's modulus E_{11} as the property of interest, corresponding to the largest eigenvalue of the second-order FOT (4.5). For details on how the Young's modulus E_{11} is computed, we refer to Appendix B. The relative bias for snapshots without optimizing the volume fraction, shown in Fig. 15(c), is on the same order of magnitude as the bias for periodized ensembles at higher values of the subsample averaging parameter κ, signified by a color progression from dark blue to lime. With optimizing the volume fraction, shown in Fig. 15(d), the bias for snapshots also reaches values comparable to periodized ensembles, but for different values of the subsample averaging parameter. While the bias for periodized ensembles is consistent with an L^{-3} decay (2.14) at a resolution of 64^3 voxels and higher, snapshots without subsample averaging are broadly consistent with an L^{-1} decay (2.15). With subsample averaging, the observed trend appears closer to an L^{-3} decay (2.14). The dispersion, both without optimizing the volume fraction, shown in Fig. 15(a), and with optimizing the volume fraction, shown in Fig. 15(b), are broadly consistent with an $L^{-3/2}$ decay (2.12). The dispersion increases with the size of the subsample averaging parameter κ. However, the dispersion is hardly lowered by optimizing the volume fraction.

For periodized ensembles, a resolution of 128^3 voxels suffices to be within 1% of the effective Young's modulus 100% of the time, shown in Tab. 8. For snapshots and no optimized volume fraction, at a higher resolution of 256^3 voxels, being within 1% of the effective Young's modulus is only achieved 40% of the time, and with optimizing the volume fraction, the probability further decreases to 29.8% in line with

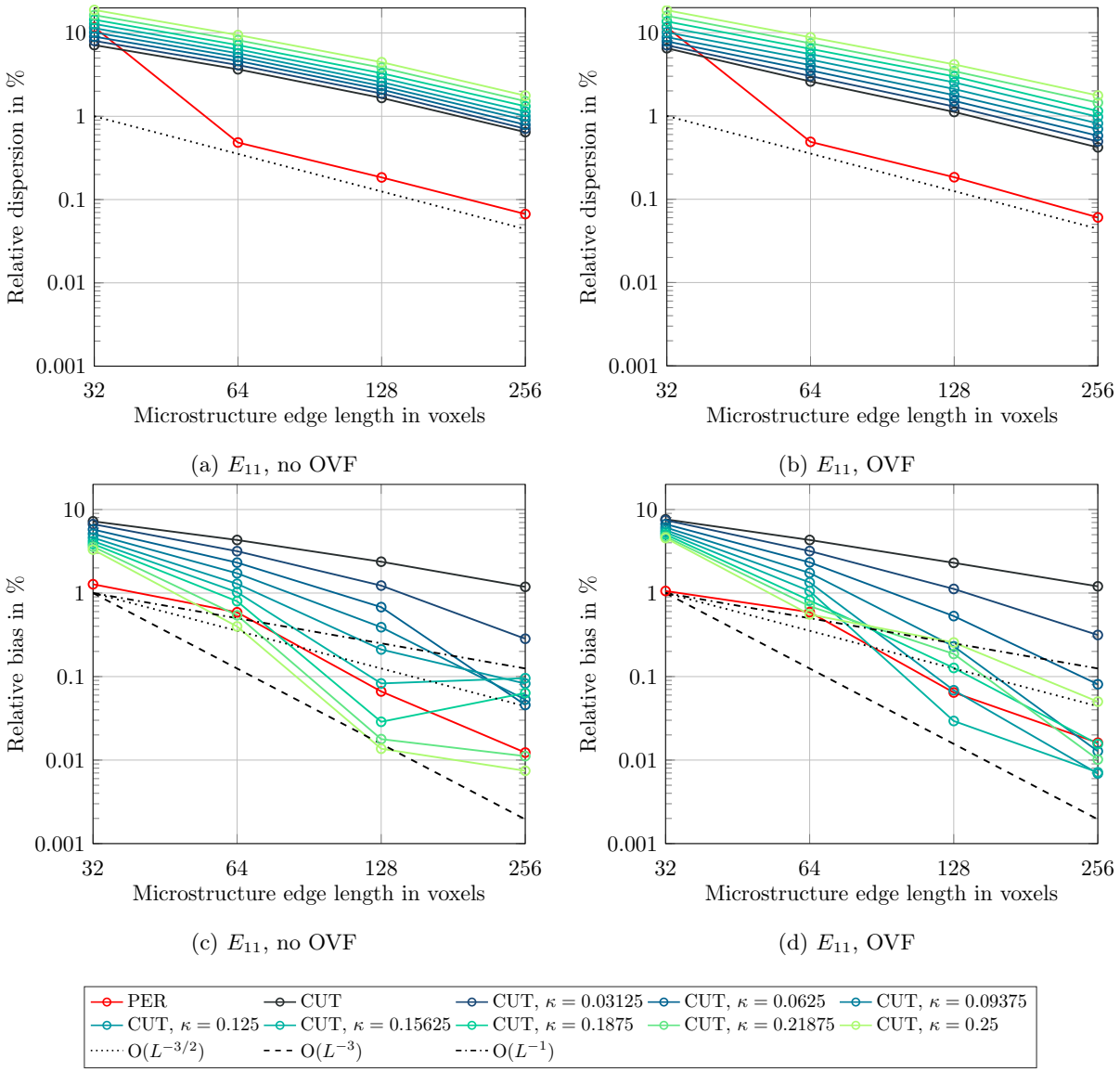

(a) E_{11}, no OVF

(b) E_{11}, OVF

(c) E_{11}, no OVF

(d) E_{11}, OVF

Figure 15: Bias and dispersion for periodic (PER) and snapshot ensembles (CUT) for fibers with orthotropic orientation (4.5)

the observations of Ravichandran et al. [16]. Using subsample averaging (2.17), the probability of being within 1% of the effective Young's modulus is increased to 80.4% with a subsample averaging mask (2.16) of $\kappa = 0.03125$ and 79.2% with $\kappa = 0.0625$ at a resolution of 256^3 voxels. Optimizing the volume fraction further increases the success rate to 92% and 92.4%, respectively.

5 Conclusion

In this work, we investigated the computation of effective elastic properties from non-periodic (snapshot) microstructures using subsample averaging and optimized volume fraction (OVF). Non-periodic microstructures arise naturally in practice, as experimental samples are necessarily finite and therefore represent (non-periodic) snapshots of an underlying random medium. This observation applies in particular to data obtained from imaging-based characterization techniques, but also more generally to experimentally observed microstructures. As a consequence, standard RVE-based homogenization in this setting suffers from a slowly decaying bias, rendering naive estimates of effective properties unreliable unless appropriate mitigation strategies are employed.

In this work, we provide the first comprehensive numerical investigation of subsample averaging for realistic microstructures beyond the theoretical setting. While recent analytical results [29] establish the potential of subsample averaging for improving convergence rates in stochastic homogenization, they are restricted to conductivity problems and do not address its practical performance in elasticity. The present study closes this gap by investigating subsample averaging for linear elastic particle-reinforced composites with industrially relevant volume fractions and material contrast.

Our results show that subsample averaging is a simple and computationally inexpensive strategy that can be readily incorporated into existing homogenization workflows without modifying the underlying solver. In particular, it provides an effective mechanism to reduce the bias associated with non-periodic microstructures. The implementation of subsample averaging is not tied to a particular microstructure-generation method. Its quantitative performance, however, may depend on the microstructure class, volume fraction, material contrast, and spatial correlation structure. Based on the results obtained, subsample averaging is therefore a promising and readily implementable option when only snapshot microstructures are available, as it significantly improves the reliability of computed effective properties when used appropriately and in combination with variance reduction techniques.

At the same time, subsample averaging introduces a fundamental limitation: Reducing the bias necessarily increases the dispersion due to the reduced averaging domain. This bias–dispersion trade-off is intrinsic to subsample averaging and implies that, when used in isolation, improvements in accuracy remain limited despite the reduction of bias.

To compensate for the increased dispersion, we combined subsample averaging with optimized volume fraction (OVF). While OVF by itself may be counterproductive for snapshot microstructures, it significantly improves accuracy when used in combination with subsample averaging. In addition to its effectiveness, OVF is a simple and computationally inexpensive strategy that can be readily applied to a wide range of inclusion-based microstructures, provided that an analytical or geometric description of the inclusions is available. In particular, the additional computational cost of the OVF procedure is negligible compared to the cost of solving the underlying homogenization problem.

In some practical settings, the volume fraction of a material is known independently, for instance from manufacturing specifications or density measurements. In such cases, volume-fraction adjustment may provide a physically motivated correction, provided that the required modification of the microstructure is consistent with the uncertainty of its characterization.

For image-based microstructures, the applicability of OVF depends on the imaging modality, phase con-

trast, segmentation uncertainty, and the availability of independent information about the bulk volume fraction. When phase assignment involves an uncertain threshold, the volume fraction may be adjusted through a controlled modification of that threshold or, where appropriate, through a geometrical procedure such as fast marching [76–78]. Such adjustments are not universally applicable and should be used only when justified by the experimental characterization.
The main findings of this work can be summarized as follows:

- Subsample averaging reduces the magnitude of the bias and produces decay trends that are more favorable than those obtained without subsample averaging.
- Subsample averaging introduces a fundamental bias–dispersion trade-off: reducing bias necessarily increases the dispersion due to the reduced averaging domain.
- Consistent subsample averaging of both stress and strain fields is essential; subsample averaging the apparent stress alone does not improve convergence rates.
- Combining subsample averaging with optimized volume fraction effectively reduces the total error and substantially improves reliability.

These findings were obtained for microstructures with spherical inclusions and fiber-reinforced composites with varying degrees of anisotropy, at realistic volume fractions. This demonstrates that the observed effects are not limited to idealized model problems which can be treated by rigorous mathematical methods [29] but persist in practically relevant settings. However, our investigation is restricted to one material system, namely a polyamide-66 matrix reinforced with E-glass inclusions. For substantially different material systems, a re-investigation of the proposed strategy may be required.
The present study focuses on linear elasticity as the fundamental case. This choice is deliberate: without a clear understanding and control of the error mechanisms in the elastic setting, extending RVE-based homogenization to more complex inelastic or nonlinear material behavior would be premature. The identification of the bias–dispersion trade-off and its mitigation therefore provides a necessary foundation for future developments in computational micromechanics.
While the proposed strategy significantly improves the reliability of computations based on snapshot microstructures, the results remain inferior to those obtained from periodized ensembles. Nevertheless, subsample averaging combined with variance reduction provides a simple and effective approach when only non-periodic samples are available, as is typically the case in practice.
The results of this work provide practical guidance for computing effective properties from non-periodic microstructures and for extending the proposed approach to experimentally obtained samples. Our findings highlight that controlling the interplay between bias and dispersion is essential for reliable RVE-based predictions. Future work will investigate alternative strategies, such as methods based on modified governing equations, which may reduce bias without increasing variance, as well as approaches that avoid reducing the averaging domain altogether. Beyond the specific setting considered here, the results highlight that controlling the interplay between bias and variance is essential for reliable multiscale simulations, particularly when working with experimentally obtained data.

Acknowledgements

TS and MS acknowledge support from the European Research Council within the Horizon Europe program - project 101040238. PB acknowledges support from Deutsche Forschungsgemeinschaft (DFG) within Priority Programme 2256 - project 441469601. Fruitful discussions with Maximilian Krause (UDE)

are acknowledged. We are grateful to the anonymous reviewers for providing detailed and constructive feedback based on a careful reading of the manuscript.

Data availability statement

The data that support the findings of this study are available from the corresponding author upon reasonable request.

A Microstructure generation

In the work at hand, short fiber-reinforced microstructures and microstructures with spherical inclusions are generated. A sphere is uniquely described by its center $\boldsymbol{x}$ and its radius r. The microstructures with monodisperse spherical inclusions are generated using the mechanical contraction method (MCM) [64]. The goal of the MCM algorithm is a random packing of N_{sph} non-overlapping spheres with volume fraction

$$\phi_{\mathrm{sph}} = \frac{4N_{\mathrm{sph}}\pi r^3}{3L^3} \tag{A.1}$$

in a cubic cell $[0, L]^3$ (2.2). The MCM proceeds by first randomly placing all spheres at a volume fraction $\phi_{\mathrm{sph},0}$ lower than the target volume fraction ϕ_{sph} and then iteratively increasing the volume fraction and removing any overlap caused by the growth of the spheres. The initial positions of the spheres are sampled pseudo-randomly from a uniform distribution. This increase in volume fraction can either be facilitated by rescaling the radius r of the spheres or by rescaling the size of the cubic cell $[0, L]^3$ together with the sphere centers $\boldsymbol{x}$. The procedure is repeated until the target volume fraction ϕ_{sph} is reached. The spheres with centers $\boldsymbol{x}_i$ and $\boldsymbol{x}_j$ must not overlap, which is encoded by the equation

$$\delta_{ij,\mathrm{sph}} \equiv \max\left(0,\ 2r + d^-_{\mathrm{sph}} - \mathrm{dist}(\boldsymbol{x}_i, \boldsymbol{x}_j)\right) = 0 \tag{A.2}$$

with some minimum distance d^-_{sph}. The distance between the centers $\mathrm{dist}(\boldsymbol{x}_i, \boldsymbol{x}_j)$ is evaluated in the periodic sense, see algorithm 1.

The overlap is removed by minimizing the objective function

Algorithm 1 periodic distance vector $\boldsymbol{d}_{\mathrm{per}}(\boldsymbol{x}_i, \boldsymbol{x}_j)$, periodic distance $\mathrm{dist}(\boldsymbol{x}_i, \boldsymbol{x}_j)$

for a=1,2,3 **do**
  $\xi_a \leftarrow x_{i,a} - x_{j,a}$
  if $(\xi_a > L/2)$ **then**
    $d_{\mathrm{per},a} \leftarrow \xi_a - L$
  else if $(\xi_a \leq -L/2)$ **then**
    $d_{\mathrm{per},a} \leftarrow \xi_a + L$
  else
    $d_{\mathrm{per},a} \leftarrow \xi_a$
  end if
end for
$\mathrm{dist}(\boldsymbol{x}_i, \boldsymbol{x}_j) \leftarrow \|\boldsymbol{d}_{\mathrm{per}}(\boldsymbol{x}_i, \boldsymbol{x}_j)\|$
return $\boldsymbol{d}_{\mathrm{per}}(\boldsymbol{x}_i, \boldsymbol{x}_j)$, $\mathrm{dist}(\boldsymbol{x}_i, \boldsymbol{x}_j)$

$$f(\boldsymbol{x}_1, \ldots, \boldsymbol{x}_{N_{\mathrm{sph}}}) = \frac{1}{2} \sum_{1 \leq i < j \leq N_{\mathrm{sph}}} \delta^2_{ij,\mathrm{sph}}. \tag{A.3}$$

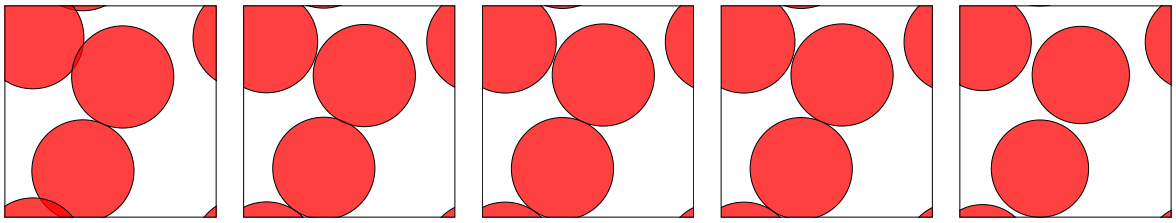

(a) Step 1 (b) Step 4 (c) Step 8 (d) Step 12 (e) Step 16

Figure 16: Mechanical contraction of three circles in a periodic cell, area fraction $\phi = 50\%$

The overlap removal of an initially overlapping configuration of three circles in a two-dimensional, periodic cell using MCM is shown in Fig. 16.

Short fibers are modeled as cylinders with a centroid $\boldsymbol{x}$ and unit direction $\boldsymbol{p}$, $\|\boldsymbol{p}\| = 1$, a length ℓ and a diameter d. All fibers live in the cubic cell (2.2) and each fiber i has the length ℓ and diameter d.

For N_{fib} fibers of equal length, the fourth order fiber orientation tensor (FOT) [74] is defined as

$$\mathbb{A}_{N_{\text{fib}}} = \frac{1}{N_{\text{fib}}} \sum_{i=1}^{N_{\text{fib}}} \boldsymbol{p}_i \otimes \boldsymbol{p}_i \otimes \boldsymbol{p}_i \otimes \boldsymbol{p}_i. \tag{A.4}$$

This tensor is linked to the elastic properties of the resulting microstructure and thus a property of interest to be prescribed to the microstructure generation algorithm [43]. The fourth order FOT is approximated by specifying the second-order FOT [74]

$$\boldsymbol{A}_{N_{\text{fib}}} = \frac{1}{N_{\text{fib}}} \sum_{i=1}^{N_{\text{fib}}} \boldsymbol{p}_i \otimes \boldsymbol{p}_i \tag{A.5}$$

and using a closure approximation $\mathbb{A}_{N_{\text{fib}}} = h(\boldsymbol{A}_{N_{\text{fib}}})$ to determine the fourth order FOT (A.4). We use the fast exact closure approximation [79].

To generate the fiber microstructures, we use the sequential addition and migration algorithm (SAM) [43], which iteratively alternates between placing some fibers $N_{\text{fib},k}$ per iteration k , sampling the positions randomly from a uniform distribution, and removing their overlap while preserving the fourth-order FOT until the desired volume fraction ϕ_{fib} is reached. We give a short summary of the algorithm to highlight how it realizes periodic microstructures and how to use it to generate snapshots instead. The total number of fibers N_{fib} is connected to the desired volume fraction ϕ_{fib} by

$$\phi_{\text{fib}} = \frac{N_{\text{fib}} \pi \ell d^2}{4L^3}. \tag{A.6}$$

To simplify the distance checks, the fibers are assumed to be spherocylinders, i.e., a fiber is modeled as a cylinder with spherical caps at the end. The distance vector between two fibers i and j is

$$\boldsymbol{k}_{ij} = s_i \frac{\ell_i}{2} \boldsymbol{p}_i - s_j \frac{\ell_j}{2} \boldsymbol{p}_j + \boldsymbol{d}_{\text{per}}(\boldsymbol{x}_i, \boldsymbol{x}_j), \tag{A.7}$$

with the centerline of a fiber parametrized via $s_i, s_j \in [-1, 1]$. The fibers must not overlap, requiring the minimum distance between two fibers i and j to satisfy the relationship

$$\delta_{ij,\text{fib}} \equiv \max\left(0,\ d + d_{\text{fib}}^{-} - \min_{s_i, s_j \in [-1,1]} \|\boldsymbol{k}_{ij}\|\right) = 0 \tag{A.8}$$

with some minimum distance d_{fib}^{-}. As with spheres, the distance vector between the centroids $\boldsymbol{d}_{\text{per}}(\boldsymbol{x}_i, \boldsymbol{x}_j)$ is evaluated in the periodic sense using algorithm 1. For the details to compute the minimum distance

we refer to Pournin et al. [80]. Both constraints of non-overlapping fibers and satisfying the prescribed FOT are encoded by the objective function

$$f(\boldsymbol{x}_1,\dots,\boldsymbol{x}_{N_{\mathrm{fib}}},\boldsymbol{p}_1,\dots\boldsymbol{p}_{N_{\mathrm{fib}}}) = \frac{1}{2}\sum_{1\le i<j\le N_{\mathrm{fib}}} \delta_{ij,\mathrm{fib}}^2 + N_{\mathrm{fib}}\frac{\varepsilon}{8}\|\mathbb{A}-\mathbb{A}_N\|^2 \tag{A.9}$$

to be minimized with the prefactor $\varepsilon = h(\ell, d)$ related to the inertia of a spherocylinder [81].

B Computing apparent material properties

The apparent stiffness $\mathbb{C}_L^{\mathrm{app}}$ acquired via solving the relationship (2.5) with the solution of the balance of linear momentum (2.3) has 21 distinct components for the fully anisotropic case and reads

$$\underline{\underline{C}}_{\mathrm{Voigt}} = \begin{bmatrix} C_{1111} & C_{1122} & C_{1133} & C_{1123} & C_{1113} & C_{1112} \\ C_{1122} & C_{2222} & C_{2233} & C_{2223} & C_{2213} & C_{2212} \\ C_{1133} & C_{2233} & C_{3333} & C_{3323} & C_{3313} & C_{3312} \\ C_{1123} & C_{2223} & C_{3323} & C_{2323} & C_{2313} & C_{2312} \\ C_{1113} & C_{2213} & C_{3313} & C_{2313} & C_{1313} & C_{1312} \\ C_{1112} & C_{2212} & C_{3312} & C_{2312} & C_{1312} & C_{1212} \end{bmatrix} \tag{B.1}$$

in Voigt's notation. For a thorough discussion we refer to Mehrabadi and Cowin [82]. The number of these distinct material parameters decreases if the material obeys further symmetries. In case of isotropy, there are two distinct material parameters, and the stiffness tensor reads

$$\underline{\underline{C}}^{\mathrm{iso}}_{\mathrm{Voigt}} = \begin{bmatrix} K+\frac{4}{3}G & K-\frac{2}{3}G & K-\frac{2}{3}G & 0 & 0 & 0 \\ K-\frac{2}{3}G & K+\frac{4}{3}G & K-\frac{2}{3}G & 0 & 0 & 0 \\ K-\frac{2}{3}G & K-\frac{2}{3}G & K+\frac{4}{3}G & 0 & 0 & 0 \\ 0 & 0 & 0 & G & 0 & 0 \\ 0 & 0 & 0 & 0 & G & 0 \\ 0 & 0 & 0 & 0 & 0 & G \end{bmatrix}. \tag{B.2}$$

in Voigt's notation with the shear modulus G and the compression modulus K. We project apparent stiffness $\mathbb{C}_L^{\mathrm{app}}$ onto the subspace of symmetric tensors. Using a suitable basis transformation such as the harmonic basis [83], the closest isotropic stiffness (B.2) to the apparent stiffness (2.5) is obtained, from which the apparent compression modulus K^{app} and apparent shear modulus G^{app} are read. The Young's modulus computes as

$$E^{\mathrm{app}} = \frac{9K^{\mathrm{app}}G^{\mathrm{app}}}{3K^{\mathrm{app}}+G^{\mathrm{app}}}. \tag{B.3}$$

For transverse isotropy, there are five distinct material parameters. A transversely isotropic stiffness tensor reads

$$\underline{\underline{C}}^{\mathrm{trans}}_{\mathrm{Voigt}} = \begin{bmatrix} C_{11} & C_{12} & C_{13} & 0 & 0 & 0 \\ C_{12} & C_{11} & C_{13} & 0 & 0 & 0 \\ C_{13} & C_{13} & C_{33} & 0 & 0 & 0 \\ 0 & 0 & 0 & C_{44} & 0 & 0 \\ 0 & 0 & 0 & 0 & C_{44} & 0 \\ 0 & 0 & 0 & 0 & 0 & \frac{1}{2}(C_{11}-C_{12}) \end{bmatrix} \tag{B.4}$$

in Voigt's notation, where we consider the z-axis as the direction of rotational symmetry. The material parameters of interest in this work, namely the longitudinal Young's modulus E_{LL} and transverse Young's

modulus E_{TT}, are obtained from the components of the inverse of the stiffness (B.4)

$$\underline{\underline{S}}^{\mathrm{trans}}_{\mathrm{Voigt}} = \begin{bmatrix} \frac{1}{E_{\mathrm{TT}}} & -\frac{\nu_{\mathrm{TT}}}{E_{\mathrm{TT}}} & -\frac{\nu_{\mathrm{LT}}}{E_{\mathrm{LL}}} & 0 & 0 & 0 \\ -\frac{\nu_{\mathrm{TT}}}{E_{\mathrm{TT}}} & \frac{1}{E_{\mathrm{TT}}} & -\frac{\nu_{\mathrm{LT}}}{E_{\mathrm{LL}}} & 0 & 0 & 0 \\ -\frac{\nu_{\mathrm{LT}}}{E_{\mathrm{LL}}} & -\frac{\nu_{\mathrm{LT}}}{E_{\mathrm{LL}}} & \frac{1}{E_{\mathrm{LL}}} & 0 & 0 & 0 \\ 0 & 0 & 0 & \frac{1}{G_{\mathrm{LT}}} & 0 & 0 \\ 0 & 0 & 0 & 0 & \frac{1}{G_{\mathrm{LT}}} & 0 \\ 0 & 0 & 0 & 0 & 0 & \frac{1}{G_{\mathrm{TT}}} \end{bmatrix}, \tag{B.5}$$

where the transformation into the harmonic basis [83] is used as an intermediate step to symmetrize and reduce the non-zero entries to the number of independent ones.
For orthotropy, nine independent material parameters arise, and the stiffness matrix assumes the form

$$\underline{\underline{C}}^{\mathrm{ortho}}_{\mathrm{Voigt}} = \begin{bmatrix} C_{11} & C_{12} & C_{13} & 0 & 0 & 0 \\ C_{12} & C_{22} & C_{23} & 0 & 0 & 0 \\ C_{13} & C_{23} & C_{33} & 0 & 0 & 0 \\ 0 & 0 & 0 & C_{44} & 0 & 0 \\ 0 & 0 & 0 & 0 & C_{55} & 0 \\ 0 & 0 & 0 & 0 & 0 & C_{66} \end{bmatrix}. \tag{B.6}$$

The material parameters of interest are the Young's moduli in the three principal directions E_{11}^{app}, E_{22}^{app} and E_{33}^{app}, which are computed from the inverse of the stiffness (B.6)

$$\underline{\underline{S}}^{\mathrm{ortho}}_{\mathrm{Voigt}} = \begin{bmatrix} \frac{1}{E_{11}} & -\frac{\nu_{21}}{E_{22}} & -\frac{\nu_{31}}{E_{33}} & 0 & 0 & 0 \\ -\frac{\nu_{12}}{E_{11}} & \frac{1}{E_{22}} & -\frac{\nu_{32}}{E_{33}} & 0 & 0 & 0 \\ -\frac{\nu_{13}}{E_{11}} & -\frac{\nu_{23}}{E_{22}} & \frac{1}{E_{33}} & 0 & 0 & 0 \\ 0 & 0 & 0 & \frac{1}{G_{23}} & 0 & 0 \\ 0 & 0 & 0 & 0 & \frac{1}{G_{13}} & 0 \\ 0 & 0 & 0 & 0 & 0 & \frac{1}{G_{12}} \end{bmatrix}. \tag{B.7}$$

As a conversion to the harmonic basis [83] does not reduce the number of non-zero entries for orthotropy, it is omitted.

C Additional Data

Tab. 5 lists the probabilities of being close to the effective properties for more values of the subsample averaging parameter κ (2.16). Periodized (PER) and snapshot microstructures (CUT) are listed, and optimizing volume fraction (3.11) for the domain Q_L of the microstructures is compared to not performing the OVF procedure.
Similarly, Tab. 6 lists the data for fiber-reinforced microstructures with isotropic orientation (4.3), Tab. 7 lists the data for fiber-reinforced microstructures with transversely isotropic orientation (4.4) and Tab. 8 lists the data for fiber-reinforced microstructures with orthotropic orientation (4.5).

Table 5: Empirical success probability to be Δ-close to E^{eff}, spherical inclusions, Young's modulus

			without OVF		with OVF	
	κ	Len.	1%-close	0.1%-close	1%-close	0.1%-close
PER	/	32	97.56 %	13.08 %	99.13 %	11.18 %
		64	100.00 %	57.73 %	100.00 %	62.30 %
		128	100.00 %	97.10 %	100.00 %	97.60 %
		256	100.00 %	100.00 %	100.00 %	100.00 %
CUT	0.00000	32	6.07 %	0.73 %	0.00 %	0.00 %
		64	10.50 %	1.37 %	0.00 %	0.00 %
		128	22.40 %	3.00 %	0.00 %	0.00 %
		256	48.00 %	6.20 %	49.80 %	0.00 %
CUT	0.03125	32	8.17 %	0.77 %	0.47 %	0.07 %
		64	20.73 %	1.97 %	42.30 %	3.53 %
		128	41.00 %	4.50 %	98.10 %	20.70 %
		256	73.60 %	8.00 %	100.00 %	43.80 %
CUT	0.06250	32	10.33 %	0.70 %	19.50 %	1.80 %
		64	22.70 %	2.13 %	49.60 %	4.77 %
		128	39.40 %	3.20 %	84.80 %	12.40 %
		256	71.20 %	7.40 %	100.00 %	24.80 %
CUT	0.09375	32	9.33 %	0.83 %	16.00 %	1.57 %
		64	20.40 %	2.33 %	35.40 %	3.17 %
		128	34.60 %	4.20 %	76.30 %	10.10 %
		256	62.60 %	5.20 %	97.60 %	15.40 %
CUT	0.12500	32	8.87 %	0.83 %	11.03 %	1.27 %
		64	20.23 %	2.47 %	29.83 %	3.17 %
		128	30.50 %	3.80 %	63.00 %	7.80 %
		256	58.40 %	5.40 %	88.80 %	11.60 %
CUT	0.15625	32	8.23 %	0.83 %	9.60 %	1.13 %
		64	18.07 %	1.37 %	25.60 %	2.60 %
		128	27.00 %	2.70 %	49.60 %	4.70 %
		256	55.20 %	5.00 %	78.60 %	10.00 %
CUT	0.18750	32	7.53 %	0.63 %	7.27 %	0.77 %
		64	17.13 %	1.83 %	21.83 %	2.17 %
		128	26.00 %	3.10 %	41.10 %	5.30 %
		256	49.40 %	6.00 %	66.00 %	5.40 %
CUT	0.21875	32	6.57 %	0.63 %	5.33 %	0.60 %
		64	14.33 %	1.60 %	18.47 %	1.83 %
		128	25.20 %	2.50 %	37.10 %	3.80 %
		256	44.20 %	5.40 %	56.00 %	7.60 %
CUT	0.25000	32	6.07 %	0.63 %	6.17 %	0.80 %
		64	11.37 %	1.17 %	15.17 %	1.63 %
		128	21.20 %	3.20 %	29.60 %	2.90 %
		256	39.40 %	4.80 %	46.00 %	4.40 %

Table 6: Empirical success probability to be Δ-close to E^{eff}, fibers with isotropic orientation (4.3), Young's modulus

			without OVF		with OVF	
	κ	Len.	1%-close	0.1%-close	1%-close	0.1%-close
PER	/	32	43.39 %	3.78 %	42.37 %	3.40 %
		64	100.00 %	15.43 %	100.00 %	14.83 %
		128	100.00 %	88.80 %	100.00 %	91.00 %
		256	100.00 %	100.00 %	100.00 %	100.00 %
CUT	0.00000	32	10.03 %	1.20 %	0.12 %	0.00 %
		64	17.30 %	1.63 %	0.00 %	0.00 %
		128	28.80 %	1.50 %	0.00 %	0.00 %
		256	66.40 %	4.80 %	100.00 %	0.00 %
CUT	0.03125	32	11.17 %	0.90 %	0.12 %	0.00 %
		64	24.20 %	2.37 %	2.40 %	0.03 %
		128	49.90 %	5.80 %	83.20 %	0.50 %
		256	90.80 %	12.00 %	100.00 %	24.80 %
CUT	0.06250	32	11.40 %	1.17 %	6.61 %	0.90 %
		64	27.03 %	2.40 %	30.93 %	2.70 %
		128	50.50 %	7.20 %	90.40 %	12.60 %
		256	90.20 %	11.60 %	100.00 %	35.80 %
CUT	0.09375	32	10.73 %	1.13 %	12.32 %	0.84 %
		64	25.43 %	2.43 %	40.33 %	4.33 %
		128	48.20 %	5.30 %	84.30 %	10.60 %
		256	85.80 %	10.80 %	100.00 %	25.00 %
CUT	0.12500	32	10.00 %	1.03 %	13.82 %	1.32 %
		64	23.27 %	2.57 %	36.27 %	3.00 %
		128	45.80 %	3.50 %	73.30 %	9.80 %
		256	81.00 %	11.00 %	96.80 %	15.60 %
CUT	0.15625	32	9.40 %	0.97 %	12.74 %	1.56 %
		64	19.30 %	2.53 %	30.03 %	2.70 %
		128	39.90 %	3.80 %	60.20 %	7.10 %
		256	74.60 %	10.60 %	92.00 %	13.40 %
CUT	0.18750	32	7.73 %	0.87 %	9.98 %	1.02 %
		64	17.20 %	1.63 %	26.83 %	3.27 %
		128	37.40 %	4.20 %	48.90 %	4.90 %
		256	69.40 %	7.40 %	83.80 %	8.60 %
CUT	0.21875	32	7.77 %	0.60 %	8.47 %	0.90 %
		64	15.17 %	1.53 %	22.27 %	2.37 %
		128	33.20 %	4.30 %	40.90 %	5.60 %
		256	64.60 %	7.60 %	73.60 %	9.60 %
CUT	0.25000	32	6.17 %	0.77 %	6.61 %	0.60 %
		64	13.80 %	1.67 %	17.23 %	1.63 %
		128	29.50 %	2.80 %	34.30 %	4.20 %
		256	58.00 %	4.80 %	63.40 %	8.60 %

Table 7: Empirical success probability to be Δ-close to E^{eff}, fibers with transversely isotropic orientation (4.4), Young's modulus

			without OVF		with OVF	
	κ	Len.	1%-close	0.1%-close	1%-close	0.1%-close
PER	/	32	6.84 %	0.83 %	6.32 %	0.67 %
		64	19.54 %	0.66 %	18.83 %	0.62 %
		128	100.00 %	23.70 %	100.00 %	20.20 %
		256	100.00 %	59.60 %	100.00 %	66.00 %
CUT	0.00000	32	4.69 %	0.37 %	2.34 %	0.13 %
		64	7.40 %	1.00 %	0.63 %	0.07 %
		128	9.10 %	0.60 %	0.40 %	0.00 %
		256	14.80 %	1.00 %	0.80 %	0.00 %
CUT	0.03125	32	5.09 %	0.70 %	3.92 %	0.32 %
		64	10.17 %	1.13 %	8.67 %	0.93 %
		128	24.00 %	2.40 %	28.50 %	3.20 %
		256	62.40 %	5.80 %	89.60 %	10.60 %
CUT	0.06250	32	5.06 %	0.55 %	4.42 %	0.38 %
		64	10.77 %	1.10 %	15.87 %	1.33 %
		128	26.90 %	2.60 %	43.70 %	4.20 %
		256	60.60 %	6.00 %	89.40 %	12.60 %
CUT	0.09375	32	5.31 %	0.33 %	6.70 %	0.63 %
		64	10.63 %	1.20 %	15.83 %	1.57 %
		128	26.00 %	3.30 %	39.00 %	4.50 %
		256	55.80 %	5.40 %	80.80 %	11.40 %
CUT	0.12500	32	5.06 %	0.44 %	6.64 %	0.76 %
		64	9.90 %	1.03 %	14.87 %	1.33 %
		128	23.00 %	2.60 %	33.30 %	3.30 %
		256	52.40 %	4.00 %	71.20 %	7.80 %
CUT	0.15625	32	4.84 %	0.62 %	6.32 %	0.70 %
		64	8.80 %	0.73 %	12.50 %	1.33 %
		128	19.40 %	1.50 %	27.20 %	2.90 %
		256	50.40 %	7.20 %	57.80 %	9.80 %
CUT	0.18750	32	4.36 %	0.59 %	4.55 %	0.44 %
		64	8.00 %	0.73 %	11.07 %	1.23 %
		128	17.60 %	1.50 %	23.40 %	2.70 %
		256	43.20 %	4.00 %	49.40 %	4.80 %
CUT	0.21875	32	3.30 %	0.44 %	4.11 %	0.13 %
		64	6.37 %	0.60 %	8.53 %	0.67 %
		128	16.00 %	1.60 %	19.80 %	2.20 %
		256	38.80 %	4.60 %	42.20 %	5.80 %
CUT	0.25000	32	2.97 %	0.18 %	3.29 %	0.38 %
		64	5.93 %	0.60 %	6.57 %	0.67 %
		128	12.20 %	1.10 %	16.10 %	1.70 %
		256	35.00 %	2.00 %	32.00 %	3.20 %

Table 8: Empirical success probability to be Δ-close to E^{eff}, fibers with orthotropic orientation (4.5), Young's modulus

			without OVF		with OVF	
	κ	Len.	1%-close	0.1%-close	1%-close	0.1%-close
PER	/	32	7.96 %	0.55 %	6.71 %	0.65 %
		64	79.99 %	8.77 %	79.65 %	7.51 %
		128	100.00 %	39.00 %	100.00 %	38.80 %
		256	100.00 %	85.00 %	100.00 %	91.40 %
CUT	0.00000	32	5.97 %	0.43 %	5.42 %	0.48 %
		64	11.20 %	1.20 %	7.80 %	0.93 %
		128	18.90 %	1.50 %	12.50 %	0.60 %
		256	40.00 %	2.40 %	29.80 %	0.40 %
CUT	0.03125	32	6.04 %	0.63 %	5.60 %	0.30 %
		64	13.07 %	1.23 %	13.73 %	1.30 %
		128	32.10 %	3.30 %	41.20 %	4.40 %
		256	80.40 %	11.80 %	92.00 %	10.80 %
CUT	0.06250	32	6.21 %	0.63 %	6.56 %	0.66 %
		64	14.70 %	1.40 %	17.27 %	2.13 %
		128	34.30 %	2.90 %	45.10 %	5.20 %
		256	79.20 %	11.40 %	92.40 %	12.80 %
CUT	0.09375	32	6.44 %	0.43 %	6.44 %	0.42 %
		64	14.90 %	1.40 %	17.80 %	1.83 %
		128	32.00 %	3.50 %	40.60 %	4.10 %
		256	69.60 %	8.80 %	86.80 %	9.20 %
CUT	0.12500	32	6.04 %	0.77 %	6.44 %	0.36 %
		64	12.83 %	1.03 %	16.20 %	1.10 %
		128	29.90 %	3.40 %	37.80 %	4.40 %
		256	67.80 %	7.80 %	81.40 %	8.20 %
CUT	0.15625	32	4.51 %	0.40 %	5.66 %	0.48 %
		64	12.83 %	1.37 %	13.30 %	1.80 %
		128	24.00 %	2.40 %	31.60 %	3.60 %
		256	61.80 %	6.40 %	71.40 %	8.40 %
CUT	0.18750	32	4.47 %	0.37 %	5.78 %	0.90 %
		64	12.00 %	1.60 %	11.43 %	1.00 %
		128	25.40 %	2.70 %	27.10 %	2.50 %
		256	56.60 %	6.40 %	63.40 %	6.60 %
CUT	0.21875	32	4.34 %	0.23 %	4.87 %	0.66 %
		64	9.90 %	1.07 %	10.27 %	0.97 %
		128	19.90 %	1.60 %	24.30 %	2.80 %
		256	51.40 %	5.20 %	49.60 %	5.40 %
CUT	0.25000	32	3.84 %	0.30 %	3.55 %	0.30 %
		64	8.67 %	1.17 %	8.90 %	0.70 %
		128	18.60 %	1.60 %	20.00 %	2.50 %
		256	43.60 %	4.80 %	38.80 %	3.00 %

References

[1] R. Hill, "Elastic properties of reinforced solids: Some theoretical principles," *Journal of the Mechanics and Physics of Solids*, vol. 11, no. 5, pp. 357–372, 1963.

[2] W. Drugan and J. Willis, "A micromechanics-based nonlocal constitutive equation and estimates of representative volume element size for elastic composites," *Journal of the Mechanics and Physics of Solids*, vol. 44, no. 4, pp. 497–524, 1996.

[3] K. Matouš, M. G. Geers, V. G. Kouznetsova, and A. Gillman, "A review of predictive nonlinear theories for multiscale modeling of heterogeneous materials," *Journal of Computational Physics*, vol. 330, pp. 192–220, 2017.

[4] I. Gitman, H. Askes, and L. Sluys, "Representative volume: Existence and size determination," *Engineering Fracture Mechanics*, vol. 74, no. 16, pp. 2518–2534, 2007.

[5] T. I. Zohdi and P. Wriggers, *An introduction to computational micromechanics*. Springer Science & Business Media, 2008.

[6] M. Kral, M. Mangan, G. Spanos, and R. Rosenberg, "Three-dimensional analysis of microstructures," *Materials Characterization*, vol. 45, no. 1, pp. 17–23, 2000.

[7] L. Tashman, L. Wang, and S. Thyagarajan, "Microstructure Characterization for Modeling HMA Behaviour using Imaging Technology," *Road Materials and Pavement Design*, vol. 8, no. 2, pp. 207–238, 2007.

[8] A. Gloria and F. Otto, "An optimal variance estimate in stochastic homogenization of discrete elliptic equations," *The Annals of Probability*, vol. 39, no. 3, pp. 779–856, 2011.

[9] A. Gloria and F. Otto, "An optimal error estimate in stochastic homogenization of discrete elliptic equations," *The Annals of Applied Probability*, vol. 22, no. 1, pp. 1–28, 2012.

[10] A. Gloria, S. Neukamm, and F. Otto, "Quantification of ergodicity in stochastic homogenization: optimal bounds via spectral gap on Glauber dynamics," *Inventiones mathematicae*, vol. 199, no. 2, pp. 455–515, 2014.

[11] T. Kanit, S. Forest, I. Galliet, V. Mounoury, and D. Jeulin, "Determination of the size of the representative volume element for random composites: statistical and numerical approach," *International Journal of Solids and Structures*, vol. 40, no. 13–14, pp. 3647–3679, 2003.

[12] Y. Efendiev, C. Kronsbein, and F. Legoll, "Multilevel Monte Carlo Approaches for Numerical Homogenization," *Multiscale Modeling and Simulation*, vol. 13, no. 4, pp. 1107–1135, 2015.

[13] N. Clozeau, M. Josien, F. Otto, and Q. Xu, "Bias in the Representative Volume Element method: Periodize the Ensemble Instead of Its Realizations," *Foundations of Computational Mathematics*, vol. 24, no. 4, pp. 1305–1387, 2023.

[14] V. Khoromskaia, B. N. Khoromskij, and F. Otto, "Numerical study in stochastic homogenization for elliptic partial differential equations: Convergence rate in the size of representative volume elements," *Numerical Linear Algebra and Applications*, vol. 27, p. e2296, 2020.

[15] M. Schneider, M. Josien, and F. Otto, "Representative volume elements for matrix-inclusion composites - a computational study on the effects of an improper treatment of particles intersecting the boundary and the benefits of periodizing the ensemble," *Journal of the Mechanics and Physics of Solids*, vol. 158, p. 104652, 2022.

[16] S. K. Ravichandran, B. H. Nguyen, and M. Schneider, "Quantifying the systematic and the random error for linear elastic particle-reinforced composites and reducing the variance by fixing the volume fraction," *Computational Mechanics*, vol. Online, pp. 1–21, 2025.

[17] K. Sab and B. Nedjar, "Periodization of random media and representative volume element size for linear composites," *Comptes Rendus Mécanique*, vol. 333, no. 2, pp. 187–195, 2005.

[18] S. Bargmann, B. Klusemann, J. Markmann, J. E. Schnabel, K. Schneider, C. Soyarslan, and J. Wilmers, "Generation of 3D representative volume elements for heterogeneous materials: A review," *Progress in Materials Science*, vol. 96, pp. 322–384, 2018.

[19] A. Mehta and M. Schneider, "A sequential addition and migration method for generating microstructures of short fibers with prescribed length distribution," *Computational Mechanics*, vol. 70, no. 4, pp. 829–851, 2022.

[20] E. Donval, M. Schneider, H. Grimm-Strele, M. Godehardt, R. Burger, P. Lechner, D. Günther, and H. Andrä, "A directional contraction method to model sand-based binder jet 3D printed materials," *International Journal of Solids and Structures*, vol. 312, p. 113260, 2025.

[21] A. Gloria, "Reduction of the resonance error - Part 1: Approximation of homogenized coefficients," *Mathematical Models and Methods in Applied Sciences*, vol. 21, no. 8, pp. 1601–1630, 2011.

[22] J.-C. Mourrat, "Efficient Methods for the Estimation of Homogenized Coefficients," *Foundations of Computational Mathematics*, vol. 19, no. 2, pp. 435–483, 2018.

[23] A. Abdulle, D. Arjmand, and E. Paganoni, "Exponential decay of the resonance error in numerical homogenization via parabolic and elliptic cell problems," *Comptes Rendus Mathematique*, vol. 357, no. 6, pp. 545–551, 2019.

[24] A. Hannukainen, J.-C. Mourrat, and H. T. Stoppels, "Computing homogenized coefficients via multiscale representation and hierarchical hybrid grids," *ESAIM: Mathematical Modelling and Numerical Analysis*, vol. 55, p. S149–S185, 2021.

[25] T. Y. Hou and X.-H. Wu, "A Multiscale Finite Element Method for Elliptic Problems in Composite Materials and Porous Media," *Journal of Computational Physics*, vol. 134, pp. 169–189, 1997.

[26] A. W. Vreman and J. G. M. Kuerten, "The filtering analog of the variational multiscale method in large-eddy simulation," *Physics of Fluids*, vol. 19, no. 9, p. 098102, 2007.

[27] Y. Efendiev and T. Y. Hou, *Multiscale Finite Element Methods: Theory and Applications*. Springer, 2009.

[28] Y. Efendiev, J. Galvis, and T. Y. Hou, "Generalized multiscale finite element methods (GMsFEM)," *Journal of Computational Physics*, vol. 251, pp. 116–135, 2013.

[29] P. Bella, J. Fischer, M. Josien, and C. Raithel, "Boundary Layer Estimates in Stochastic Homogenization," *arXiv:2403.12911*, pp. 1–48, 2024.

[30] X. Blanc and C. Le Bris, "Improving on computation of homogenized coefficients in the periodic and quasi-periodic settings," *Networks and Heterogeneous Media*, vol. 5, no. 1, pp. 1–29, 2010.

[31] J. Segurado and J. LLorca, "Computational micromechanics of composites: The effect of particle spatial distribution," *Mechanics of Materials*, vol. 38, no. 8–10, pp. 873–883, 2006.

[32] P. Kanouté, D. P. Boso, J. L. Chaboche, and B. A. Schrefler, "Multiscale methods for composites: A review," *Archives of Computational Methods in Engineering*, vol. 16, no. 1, pp. 31–75, 2009.

[33] J. Yvonnet, *Computational Homogenization of Heterogeneous Materials with Finite Elements*. Springer, 2019.

[34] H. Moulinec and P. Suquet, "A fast numerical method for computing the linear and nonlinear mechanical properties of composites," *Comptes Rendus de l'Académie des Sciences. Série II*, vol. 318, no. 11, pp. 1417–1423, 1994.

[35] H. Moulinec and P. Suquet, "A numerical method for computing the overall response of nonlinear composites with complex microstructure," *Computer Methods in Applied Mechanics and Engineering*, vol. 157, pp. 69–94, 1998.

[36] M. Schneider, "A review of nonlinear FFT-based computational homogenization methods," *Acta Mechanica*, vol. 232, no. 6, pp. 2051–2100, 2021.

[37] S. Lucarini, M. V. Upadhyay, and J. Segurado, "FFT based approaches in micromechanics: fundamentals, methods and applications," *Modelling and Simulation in Materials Science and Engineering*, vol. 30, no. 2, p. 023002, 2021.

[38] C. Ye and E. T. Chung, "Convergence of trigonometric and finite-difference discretization schemes for FFT-based computational micromechanics," *BIT Numerical Mathematics*, vol. 63, p. 11, 2023.

[39] M. Schneider, "Superaccurate effective elastic moduli via postprocessing in computational homogenization," *International Journal for Numerical Methods in Engineering*, vol. 123, no. 17, pp. 4119–4135, 2022.

[40] M. Schneider and D. Wicht, "Superconvergence of the effective Cauchy stress in computational homogenization of inelastic materials," *International Journal for Numerical Methods in Engineering*, vol. 124, no. 4, pp. 959–978, 2023.

[41] F. Gehrig, D. Wicht, M. Krause, and T. Böhlke, "FFT-based investigation of the shear stress distribution in face-centered cubic polycrystals," *International Journal of Plasticity*, vol. 157, p. 103369, 2022.

[42] M. Schneider, T. Hofmann, H. Andrä, P. Lechner, F. Ettemeyer, W. Volk, and H. Steeb, "Modelling the microstructure and computing effective elastic properties of sand core materials," *International Journal of Solids and Structures*, vol. 143, pp. 1–17, 2018.

[43] M. Schneider, "The sequential addition and migration method to generate representative volume elements for the homogenization of short fiber reinforced plastics," *Computational Mechanics*, vol. 59, no. 2, pp. 247–263, 2016.

[44] A. Prakash and R. A. Lebensohn, "Simulation of micromechanical behavior of polycrystals: finite elements versus fast Fourier transforms," *Modelling and Simulation in Materials Science and Engineering*, vol. 17, no. 6, p. 064010, 2009.

[45] J. Zeman, T. W. J. de Geus, J. Vondřejc, R. H. J. Peerlings, and M. G. D. Geers, "A finite element perspective on nonlinear FFT-based micromechanical simulations," *International Journal for Numerical Methods in Engineering*, vol. 111, pp. 903–926, 2017.

[46] Z. Chen, Y. M. Xie, Z. Wang, Q. Li, X. Wu, and S. Zhou, "A comparison of fast Fourier transform-based homogenization method to asymptotic homogenization method," *Composite Structures*, vol. 238, p. 111979, 2020.

[47] L. Risthaus and M. Schneider, "Imposing Dirichlet boundary conditions directly for FFT-based computational micromechanics," *Computational Mechanics*, vol. 74, pp. 1089–1113, 2024.

[48] L. Risthaus and M. Schneider, "FFT-based computational micromechanics with Dirichlet boundary conditions on the rotated staggered grid," *International Journal for Numerical Methods in Engineering*, vol. 125, no. 21, p. e7569, 2024.

[49] L. Risthaus and M. Schneider, "Robust and Efficient FFT-Based Solvers for Unit-Cell Problems With Voids and Pores Under Displacement Boundary Conditions," *International Journal for Numerical Methods in Engineering*, vol. 126, no. 18, p. e70124, 2025.

[50] C. Le Bris, F. Legoll, and W. Minvielle, "Special quasirandom structures: A selection approach for stochastic homogenization," *Monte Carlo Methods and Applications*, vol. 22, no. 1, pp. 25–54, 2016.

[51] X. Blanc, C. Le Bris, and F. Legoll, "Some variance reduction methods for numerical stochastic homogenization," *Philosophical Transactions of the Royal Society A: Mathematical, Physical and Engineering Sciences*, vol. 374, no. 2066, p. 20150168, 2016.

[52] J. Fischer and S. Neukamm, "Optimal Homogenization Rates in Stochastic Homogenization of Nonlinear Uniformly Elliptic Equations and Systems," *Archive for Rational Mechanics and Analysis*, vol. 242, no. 1, pp. 343–452, 2021.

[53] S. Brisard, M. Bertin, and F. Legoll, "A variance reduction strategy for numerical random homogenization based on the equivalent inclusion method," *Computer Methods in Applied Mechanics and Engineering*, vol. 417, p. 116389, 2023.

[54] J. Mandel, "Contribution théorique à l'étude de l'écrouissage et des lois de l'écoulement plastique," in *Applied Mechanics*, pp. 502–509, 1966.

[55] G. C. Papanicolaou and S. R. S. Varadhan, "Boundary value problems with rapidly oscillating random coefficients," in *Random fields, Vol. I, II (Esztergom, 1979)*, vol. 27 of *Colloq. Math. Soc. János Bolyai*, pp. 835–873, North-Holland, Amsterdam-New York, 1981.

[56] V. V. Zhikov, S. M. Kozlov, and O. A. Oleinik, *Homogenization of Differential Operators and Integral Functionals*. New York: Springer-Verlag, 1994.

[57] A. Bourgeat and A. Pianitski, "Approximations of effective coefficients in stochastic homogenization," *Annales de l'Institut Henri Poincare (B) Probability and Statistics*, vol. 40, no. 2, pp. 153–165, 2004.

[58] H. Owhadi, "Approximation of the effective conductivity of ergodic media by periodization," *Probability Theory and Related Fields*, vol. 125, pp. 225–258, 2003.

[59] M. Duerinckx, A. Gloria, and F. Otto, "The Structure of Fluctuations in Stochastic Homogenization," *Communications in Mathematical Physics*, vol. 377, no. 1, pp. 259–306, 2020.

[60] J. Dirrenberger, S. Forest, and D. Jeulin, "Towards gigantic RVE sizes for 3D stochastic fibrous networks," *International Journal of Solids and Structures*, vol. 51, no. 2, pp. 359–376, 2014.

[61] D. Jeulin, "Power Laws Variance Scaling of Boolean Random Varieties," *Methodology and Computing in Applied Probability*, vol. 18, no. 4, pp. 1065–1079, 2015.

[62] A. Gloria and Z. Habibi, "Reduction in the Resonance Error in Numerical Homogenization II: Correctors and Extrapolation," *Foundations of Computational Mathematics*, vol. 16, no. 1, pp. 217–296, 2015.

[63] G. W. Milton, *The Theory of Composites*. Cambridge: Cambridge University Press, 2002.

[64] S. R. Williams and A. P. Philipse, "Random packings of spheres and spherocylinders simulated by mechanical contraction," *Physical Review E*, vol. 67, no. 5, pp. 1–9, 2003.

[65] J. Fischer, "The Choice of Representative Volumes in the Approximation of Effective Properties of Random Materials," *Archive for Rational Mechanics and Analysis*, vol. 234, no. 2, pp. 635–726, 2019.

[66] J. Zeman, J. Vondřejc, J. Novák, and I. Marek, "Accelerating a FFT-based solver for numerical homogenization of periodic media by conjugate gradients," *Journal of Computational Physics*, vol. 229, no. 21, pp. 8065–8071, 2010.

[67] L. Gélébart and R. Mondon-Cancel, "Non-linear extension of FFT-based methods accelerated by conjugate gradients to evaluate the mechanical behavior of composite materials," *Computational Materials Science*, vol. 77, pp. 430–439, 2013.

[68] N. Lahellec, J. C. Michel, H. Moulinec, and P. Suquet, "Analysis of Inhomogeneous Materials at Large Strains using Fast Fourier Transforms," in *IUTAM Symposium on Computational Mechanics of Solid Materials at Large Strains*, pp. 247–258, 2003.

[69] M. Schneider, "A dynamical view of nonlinear conjugate gradient methods with applications to FFT-based computational micromechanics," *Computational Mechanics*, vol. 66, no. 1, pp. 239–257, 2020.

[70] M. Schneider, "On the Barzilai-Borwein basic scheme in FFT-based computational homogenization," *International Journal for Numerical Methods in Engineering*, vol. 118, no. 8, pp. 482–494, 2019.

[71] M. Schneider, F. Ospald, and M. Kabel, "Computational homogenization of elasticity on a staggered grid," *International Journal for Numerical Methods in Engineering*, vol. 105, no. 9, pp. 693–720, 2015.

[72] P. A. Hessman, F. Welschinger, K. Hornberger, and T. Böhlke, "On mean field homogenization schemes for short fiber reinforced composites: Unified formulation, application and benchmark," *International Journal of Solids and Structures*, vol. 230–231, p. 111141, 2021.

[73] H. Altendorf, D. Jeulin, and F. Willot, "Influence of the fiber geometry on the macroscopic elastic and thermal properties," *International Journal of Solids and Structures*, vol. 51, no. 23–24, pp. 3807–3822, 2014.

[74] S. G. Advani and C. L. Tucker, "The Use of Tensors to Describe and Predict Fiber Orientation in Short Fiber Composites," *Journal of Rheology*, vol. 31, no. 8, pp. 751–784, 1987.

[75] J. K. Bauer, M. Schneider, and T. Böhlke, "On the Phase Space of Fourth-Order Fiber-Orientation Tensors," *Journal of Elasticity*, vol. 153, pp. 161–184, 2023.

[76] S. Osher and J. A. Sethian, "Fronts Propagating with Curvature-Dependent Speed: Algorithms Based on Hamilton-Jacobi Formulations," *Journal of Computational Physics*, vol. 79, pp. 12–49, 1988.

[77] J. A. Sethian, "A Fast Marching Level Set Method for Monotonically Advancing Fronts," *Proceedings of the National Academy of Sciences of the United States of America*, vol. 93, pp. 1591–1595, 1996.

[78] J. A. Sethian, *Level Set Methods and Fast Marching Methods: Evolving Interfaces in Computational Geometry, Fluid Mechanics, Computer Vision, and Materials Science*. Cambridge Monographs on Applied and Computational Mathematics, Cambridge University Press, 1999.

[79] S. Montgomery-Smith, D. Jack, and D. E. Smith, "The Fast Exact Closure for Jeffery's equation with diffusion," *Journal of Non-Newtonian Fluid Mechanics*, vol. 166, no. 7–8, pp. 343–353, 2011.

[80] L. Pournin, M. Weber, M. Tsukahara, J.-A. Ferrez, M. Ramaioli, and T. M. Liebling, "Three-dimensional distinct element simulation of spherocylinder crystallization," *Granular Matter*, vol. 7, no. 2–3, pp. 119–126, 2005.

[81] A. G. García, "Random packings via mechanical contraction," Master's thesis, Universiteit Utrecht, the Netherlands, 2015.

[82] M. M. Mehrabadi and S. C. Cowin, "Eigentensors of Linear Anisotropic Elastic Materials," *The Quarterly Journal of Mechanics and Applied Mathematics*, vol. 43, no. 1, pp. 15–41, 1990.

[83] M. Krause and T. Böhlke, "Tensorial harmonic bases of arbitrary order with applications in elasticity, elastoviscoplasticity and texture-based modeling," *Mathematics and Mechanics of Solids*, vol. 30, no. 5, pp. 1188–1212, 2024.